


UDP-glucose dehydrogenase expression is upregulated following EMT and differentially affects intracellular glycerophosphocholine and acetylaspartate levels in breast mesenchymal cell lines

Qiong Wang¹, Sigurdur Trausti Karvelsson¹, Freyr Johannsson¹, Arnar Ingi Vilhjalmsón¹, Lars Hagen^{2,3,4}, Davi de Miranda Fonseca^{2,3,4}, Animesh Sharma^{2,3,4}, Geir Slupphaug^{2,3,4} and Ottar Rolfsson¹ 

1 Center for Systems Biology, Biomedical Center, Faculty of Medicine, School of Health Sciences, University of Iceland, Reykjavik, Iceland

2 Department of Clinical and Molecular Medicine, Norwegian University of Science and Technology, NTNU, Trondheim, Norway

3 Clinic of Laboratory Medicine, St. Olavs Hospital, Trondheim, Norway

4 PROMEC Core Facility for Proteomics and Modomics, Norwegian University of Science and Technology, NTNU, and the Central Norway Regional Health Authority Norway, Trondheim, Norway

Keywords

acetylaspartate; breast cancer; EMT; glycerophosphocholine; PDGFRB; UGDH

Correspondence

O. Rolfsson, Center for Systems Biology, Biomedical Center, Faculty of Medicine, School of Health Sciences, University of Iceland, Sturlugata 8, 101 Reykjavik, Iceland
Tel: +354 5255854
E-mail: ottarr@hi.is

(Received 6 August 2021, revised 4 November 2021, accepted 21 December 2021)

doi:10.1002/1878-0261.13172

Metabolic rewiring is one of the indispensable drivers of epithelial–mesenchymal transition (EMT) involved in breast cancer metastasis. In this study, we explored the metabolic changes during spontaneous EMT in three separately established breast EMT cell models using a proteomic approach supported by metabolomic analysis. We identified common proteomic changes, including the expression of CDH1, CDH2, VIM, LGALS1, SERPINE1, PKP3, ATP2A2, JUP, MTCH2, RPL26L1 and PLOD2. Consistently altered metabolic enzymes included the following: FDFT1, SORD, TSTA3 and UDP-glucose dehydrogenase (UGDH). Of these, UGDH was most prominently altered and has previously been associated with breast cancer patient survival. siRNA-mediated knock-down of *UGDH* resulted in delayed cell proliferation and dampened invasive potential of mesenchymal cells and downregulated expression of the EMT transcription factor SNAI1. Metabolomic analysis revealed that siRNA-mediated knock-down of *UGDH* decreased intracellular glycerophosphocholine (GPC), whereas levels of acetylaspartate (NAA) increased. Finally, our data suggested that platelet-derived growth factor receptor beta (PDGFRB) signalling was activated in mesenchymal cells. siRNA-mediated knock-down of *PDGFRB* downregulated *UGDH* expression, potentially via NFκB-p65. Our results support an unexplored relationship between UGDH and GPC, both of which have previously been independently associated with breast cancer progression.

Abbreviations

AGC, automatic gain control; ATP2A2, sarcoplasmic/endoplasmic reticulum calcium ATPase 2; CD44, CD44 antigen; CDH1, E-cadherin; CDH2, N-cadherin; EGFR, epidermal growth factor receptor; EMT, epithelial–mesenchymal transition; FDFT1, squalene synthase; FDR, false discovery rate; FLNA, filamin-A; FSCN1, fascin; GEMs, genome-scale metabolic network reconstructions; GPC, glycerophosphocholine; HBP, hexosamine biosynthesis pathway; JUP, junction plakoglobin; LGALS1, galectin-1; LMNB1, Lamin-B1; MSN, moesin; MTCH2, mitochondrial carrier homolog 2; NAA, acetylaspartate; NDRG1, N-myc downstream regulated 1; PDGFRB, platelet-derived growth factor receptor beta; pERK, extracellular signal-regulated kinase (phosphorylated); PKP3, plakophilin-3; PLA2G15, phospholipase A2 group XV; PLOD2, procollagen-lysine,2-oxoglutarate; PPAR γ , peroxisome proliferator-activated receptor γ ; PSM, peptide-spectrum matches; RELA (NFκB-p65), nuclear factor NF-kappa-B p65 subunit; RPL26L1, 60S ribosomal protein L26-like 1; S100A2, S100 calcium-binding protein A2; SERPINE1, plasminogen activator inhibitor 1; SNAI1, Snail family transcriptional repressor 1; SORD, sorbitol dehydrogenase; TLN1, Talin-1; TSTA3, GDP-L-fucose synthase; UDP-Glc, UDP-glucose; UDP-GlcA, UDP-glucuronate; UGDH, UDP-glucose dehydrogenase; VIM, vimentin.

	D492-D492M	HMLE-HMLEM	PMC42LA-PMC42ET
Tissue	Breast reduction mammoplasty	Breast reduction mammoplasty	Breast; derived from metastatic site: pleural effusion
Immortalization	HPV-16 E6/E7 gene transduction	hTERT and SV-40 Large T antigen expression	N/A
Cell type	Basal-like; with stem cell properties	Luminal and basal epithelial cells	Express secretory and myoepithelial markers
Induce EMT	Spontaneous EMT; Co-culture with endothelial cells	Spontaneous EMT; Trypsinization	Spontaneous MET; Treatment with a combination of hormones to induce MET
Tumorigenicity	Non-tumorigenic	Non-tumorigenic	Non-tumorigenic

Fig. 1. Summary of the three breast EMT cell models. Comparison of the three breast EMT cell models with respect to tissue origin, immortalization methods, cell markers, EMT induction methods and tumorigenicity.

USA; I6634), 10 $\mu\text{g}\cdot\text{mL}^{-1}$ transferrin (Merck; T2252), 10 $\text{ng}\cdot\text{mL}^{-1}$ EGF (PeproTech, Cranbury, NJ, USA; AF-100-15), 2.6 $\text{ng}\cdot\text{mL}^{-1}$ Na-selenite (BD Biosciences, San Jose, CA, USA; 354201), 10^{-10} M estradiol (Sigma, St. Louis, MO, USA; E2758), 1.4×10^{-6} M hydrocortisone (Sigma; H0888), 0.15 IU prolactin (PeproTech; 100-07), 100 IU penicillin and 0.1 $\text{mg}\cdot\text{mL}^{-1}$ streptomycin (Gibco™, TFS; 15140122) and 2 mM glutamine (TFS; 25030024). The passage numbers for both D492 and D492M were from 31, while D492HER2 was cultured from passage 65. HMLE was isolated from reduction mammoplasties [12], while HMLEM was generated from HMLE via differential trypsinization [7]. The HMLE cell lines (HMLE with passage number from 16 and HMLEM with passage number from 28) were cultured in serum-free DMEM/F-12 medium supplemented with 10 $\mu\text{g}\cdot\text{mL}^{-1}$ insulin, 10 $\text{ng}\cdot\text{mL}^{-1}$ EGF, 1.4×10^{-6} M hydrocortisone, 100 IU penicillin and 0.1 $\text{mg}\cdot\text{mL}^{-1}$ streptomycin and 2 mM glutamine. PMC42ET was originally established from pleural effusion from the metastatic site in a breast cancer patient [15], and PMC42LA was then generated via mesenchymal-epithelial transition by hormone treatments [13]. The PMC42 cell lines (PMC42LA and PMC42ET with passage numbers from 9) were cultured in RPMI 1640 Medium (TFS; 52400025) supplemented with 10% FBS (Gibco™ 10270106) and 100 IU penicillin and 0.1 $\text{mg}\cdot\text{mL}^{-1}$ streptomycin. The antibiotics were excluded in the medium for the transient knock-

experiment, DMEM/F-12 was replaced by ‘DMEM:F-12 for SILAC’ (TFS; 88370) with light- (L-arginine, L-lysine), medium- [L-arginine- $^{13}\text{C}_6$ hydrochloride (Arg + 6 Da), L-lysine-4,4,5,5-d4 hydrochloride (Lys + 4 Da)] or heavy- (L-arginine- $^{13}\text{C}_6$, $^{15}\text{N}_4$ hydrochloride (Arg + 10 Da), L-lysine- $^{13}\text{C}_6$, $^{15}\text{N}_2$ hydrochloride (Lys + 8 Da)] labelled arginine or lysine (Cambridge Isotope Laboratories, Tewksbury, MA, USA). In the invasion assay, H14 was supplemented with 10% FBS in the lower chamber of the Transwell. The MDA-MB-231 cells (passage number 26) were cultured in RPMI 1640 supplemented with 10% FBS and 100 IU penicillin and 0.1 $\text{mg}\cdot\text{mL}^{-1}$ streptomycin. All cell lines were cultured at 37 °C with 5% CO_2 for routine maintenance, and cells were routinely checked for mycoplasma contamination. All cell lines used in this study were kindly provided by the Stem Cell Research Unit, Biomedical Center, University of Iceland.

2.2. LFQ proteomics and SILAC phosphoproteomic analysis

The proteomic experimental set-up was illustrated in Fig. S1A.

2.2.1. LFQ protein and peptide sample preparation

Cells were lysed with 4% sodium dodecyl sulfate

in a breast cancer patient [15], and PMC42LA was then generated via mesenchymal–epithelial transition by hormone treatments [13]. The PMC42 cell lines (PMC42LA and PMC42ET with passage numbers from 9) were cultured in RPMI 1640 Medium (TFS; 52400025) supplemented with 10% FBS (Gibco™ 10270106) and 100 IU penicillin and 0.1 mg·mL⁻¹ streptomycin. The antibiotics were excluded in the medium for the transient knock-down experiments. In the SILAC phosphoproteomic

2.2. LFQ proteomics and SILAC phosphoproteomic analysis

The proteomic experimental set-up was illustrated in Fig. S1A.

2.2.1. LFQ protein and peptide sample preparation

Cells were lysed with 4% sodium dodecyl sulfate (SDS; MP Biomedicals™, Irvine, CA, USA) in

100 mM Tris (Sigma) and kept on ice for 10 min and then transferred to 1.5-mL Eppendorf tubes. After five freeze/thaw (-80°C /room temperature) cycles, the samples were centrifuged at 20 817 *g* for 20 min at 4°C . The supernatants were collected and aliquoted in new tubes and stored at -80°C . Total protein was quantified with the Pierce™ BCA protein assay (TFS). A volume containing 12–15 μg total protein was precipitated by chloroform/methanol precipitation and reconstituted in 50 mM ammonium bicarbonate. The protein sample was reduced with 1 M dithiothreitol (DTT) for 20 min at 70°C and then alkylated by 200 mM iodoacetamide (IAM) at room temperature in the dark for 30 min, followed by quenching the extra IAM with 1 M DTT for 20 min at room temperature in the dark. Samples were digested overnight with 1.5 μg trypsin at 37°C . Tryptic peptides were desalted using C-18 StageTips as described [39], after which peptides were dried in a SpeedVac centrifuge and resuspended in 0.1% formic acid.

2.2.2. LFQ LC-MS/MS analysis

Peptides were analysed on an LC-MS/MS platform consisting of an Easy-nLC 1200 UHPLC system (TFS) interfaced with a QExactive HF Orbitrap Mass Spectrometer (TFS) via a nanospray ESI ion source (TFS). Peptides were injected into a C-18 trap column (Acclaim PepMap100, 75 μm i. d. \times 2 cm, C-18, 3 μm , 100 \AA ; TFS) and further separated on a C-18 analytical column (Acclaim PepMap100, 75 μm i. d. \times 50 cm, C-18, 2 μm , 100 \AA ; TFS) using a multi-step gradient with buffer A (0.1% formic acid) and buffer B (80% CH_3CN , 0.1% formic acid): from 2% to 10% buffer B in 10 min, 10% to 50% buffer B in 130 min, 50% to 100% buffer B in 20 min and 20 min with 100% buffer B. The HPLC was re-equilibrated with 2% buffer B before the next injection. The flow rate was 250 $\text{nL}\cdot\text{min}^{-1}$. Peptides eluted were analysed on QExactive HF mass spectrometer (TFS) operating in positive ion- and data-dependent acquisition mode using the following parameters: electrospray voltage 1.9 kV, HCD fragmentation with normalized collision energy 29, automatic gain control (AGC) target value of 3×10^6 for Orbitrap MS and 1×10^5 for MS/MS scans. Each MS scan (m/z 350–1650) was acquired at a resolution of 120 000 FWHM, followed by 15 MS/MS scans triggered for AGC targets above 2×10^3 , at a maximum ion injection time of 100 ms for MS and 100 ms for MS/MS scans. The proteomic method has been described previously [40].

2.2.3. LFQ protein and peptide identification and quantification

Proteins were identified and quantified by processing MS data using Thermo Scientific™ PROTEOME DISCOVERER™ (PD, version 2.3; TFS). PREVIEW version 2.3.5 (Protein Metrics Inc.) [41] was used to inspect the raw files to determine optimal search criteria, and the following search parameters were used: (a) enzyme specified as trypsin with maximum of two missed cleavages allowed; (b) acetylation of protein N-terminal including loss-of-methionine; (c) oxidation of methionine; (d) deamidation of asparagine/glutamine as dynamic post-translational modification; (e) carbamidomethylation of cysteine as static; Precursor mass-tolerance of 10 PPM while fragment mass-tolerance of 0.02 Dalton. PD's node, Spectrum file RC, was set up to query the raw files against the human proteome downloaded from UniProt (*Homo sapiens*, UP000005640, October 2018) with the static modification to recalibrate and detect features with the Minora node. Further, the internal contaminant database was also queried along with the human proteome using Sequest [42] search engine available in PD. For downstream analysis of these peptide-spectrum matches (PSM), both protein and peptide identifications/PSM false discovery rate (FDR) were set to 1%; thus, only the unique peptides with high confidence were used for final protein group identification. Peak abundances were extracted by integrating the area under the peak curve. Each protein group abundance was normalized by the total abundance of all identified peptides at $\text{FDR} < 1\%$. Summed up median values for all unique peptide ion abundances mapped to respective protein using label-free quantification scaled on all average with Precursor Ion Quantifier node [43] for PD were used.

The mass spectrometry proteomic data have been deposited to the ProteomeXchange Consortium via the PRIDE [44] partner repository with the data set identifier PXD024164.

The protocol for SILAC phosphoproteomic analysis was thoroughly described in the other study [26]. Briefly, protein sample equivalent to 4 mg was dissolved and fractionated, followed by phosphorylated peptide enrichment with MagReSyn-TiIMAC beads (Resyn Biosciences, Edenvale, Gauteng, South Africa) and Magnetic Rack (DynaMag-2; Life Technologies, Carlsbad, CA, USA). Analyses of peptides for total proteome and phosphorylated proteome were carried out on a Velos-Pro Orbitrap (TFS) mass spectrometer coupled with a Dionex UltiMate 3000 RS (TFS). The raw data files obtained from the mass spectrometric outputs for each experiment were merged into a single quantitated data set using MAXQUANT (version 1.5.2.8)

[45] and the ANDROMEDA search engine software [46]. The mass spectrometry phosphoproteomic data have been deposited to the ProteomeXchange Consortium via the PRIDE [44] partner repository with the data set identifier PXD025858.

2.3. Metabolomic analysis

The metabolomic experimental set-up was illustrated in Fig. S1A. Cells were washed with saline solution (0.9%), and the metabolites were extracted with MeOH : dH₂O (80 : 20) containing an internal standard mix (Table S1). After adding MeOH : dH₂O (80 : 20), samples were centrifuged, and the supernatant was taken and vacuum dried. The extracts were analysed on UPLC mass spectrometry (SYNAPT G2; Waters) according to published protocols [47]. Metabolites were identified and quantified in MASSLYNX software (version 4.2) from waters. For untargeted data analysis, xCMS [48] was used for automatic peak-picking (centWave) [49] and retention time alignment (OBI-Warp) [50]. All features that eluted in the first 66 s were omitted from further analysis. Feature intensities were normalized using quality control sample-based robust LOESS (locally estimated scatterplot smoothing) signal correction (QC-RLSC) [51] which was implemented using the R-package *NormalizeMets* [52]. For quality assurance, all features with over 25% relative standard deviation in the QC samples were omitted from further analysis. Generalized logarithmic transformation (glog) [53] and autoscaling were used to obtain mean-centred, normally distributed feature intensity values with equal variance. The expression of metabolites was normalized to cell numbers estimated by crystal violet assays. For the normalization of the metabolic measurements in the metabolomic experiment, cells were counted using a crystal violet assay. In short, cells were fixed with 100% cold MeOH and stained with 0.25% crystal violet (Merck; C.I. 42555). After washing, stained cells were dissolved into 100 μ L of 10% acetic acid and measured at 570 nm in the microplate reader (SpectraMax[®] M3; Molecular Devices LLC, San Jose, CA, USA).

2.4. siRNA transient knock-down and quantitative reverse transcription PCR

Cells were seeded either at 60 000 cells/well in 48-well plates or at 480 000 cells/well in 6-well plates. Before cell seeding, plates were coated with respective control siRNA (Silencer[™] Select Negative Control, 4390843) and target siRNA (Silencer[™] Select siUGDH: s409 and s410; siPDGFRB: s10240; siRELA: s11914 and

Transfection Reagent (TFS). Cells were transfected at 37 °C and 5% CO₂ for 48 h with the final siRNA concentration of 10 nM.

In the RT-qPCR experiments, cells were cultured in 48-well plates for 72 h, followed by total RNA extraction with TRI Reagent[™] Solution (Invitrogen[™], TFS). RNA concentration was determined in NanoDrop One (TFS). 500–1000 ng of RNA was used for cDNA synthesis on the thermal cycler (Peltier Thermal Cycler, MJ research, PTC-225, Alameda, CA, USA) using High-Capacity cDNA Reverse Transcription Kit (TFS). Gene expression was measured with SYBR Green (Luna[®] Universal qPCR Master Mix; New England BioLabs, Ipswich, MA, USA) on Bio-Rad CFX384 Touch[™] Real-Time PCR Detection System (Bio-Rad, Hercules, CA, USA). Primers were either selected from Primer-Bank, designed on the Primer3Plus website, or based on the literature. Primer sequences for genes studied in this study were listed in Table S2.

2.5. Cell proliferation assay

Cells in quadruplicate were seeded at 10 000 cells/well in 96-well plates. *UGDH* knock-down followed the methods described above. For D492M, 24 h after seeding (48 h for D492HER2), cells were placed under the microscope (LEICA CTR 6500, bright field, 10 \times) at 37 °C with 5% CO₂ for real-time monitoring and multiple data acquisition. The microscope was controlled by software MICRO-MANAGER (version 1.4.22, Vale's laboratory, San Francisco, CA, USA). Three spots were chosen in each well, and photographs were taken every 6 h. Cell growth was monitored for 66 h for D492M while 42 h for D492HER2. Photographs were batch-processed with Macro in software IMAGEJ 1.52p (NIH, Bethesda, MD, USA), and cell numbers were normalized to the starting point.

2.6. Transwell invasion assay

The D492M and D492HER2 cells were cultured with siRNA transfection (Scramble and siUGDH) for 48 h in 6-well plates. *UGDH* knock-down followed the methods described above. Cells were then reseeded into filter units (Falcon[®] Permeable Support for 24-well Plate with 8.0- μ m Transparent PET Membrane, 353097, Corning, NY, USA) coated with Matrigel (Corning[®] Matrigel[®] Matrix, 356234) at a density of 30 000 cells/well. First, the filter inserts were coated with 100 μ L 1 : 10 diluted Matrigel for 20–30 min at 37 °C. Next, 300 μ L of cell suspension was added on top of the filter units. Then, 500 μ L of H14 medium

2.4. siRNA transient knock-down and quantitative reverse transcription PCR

Cells were seeded either at 60 000 cells/well in 48-well plates or at 480 000 cells/well in 6-well plates. Before cell seeding, plates were coated with respective control siRNA (Silencer™ Select Negative Control, 4390843) and target siRNA (Silencer™ Select siUGDH: s409 and s410; siPDGFRB: s10240; siRELA: s11914 and s11915) as well as Lipofectamine™ RNAiMAX

into filter units (Falcon® Permeable Support for 24-well Plate with 8.0-µm Transparent PET Membrane, 353097, Corning, NY, USA) coated with Matrigel (Corning® Matrigel® Matrix, 356234) at a density of 30 000 cells/well. First, the filter inserts were coated with 100 µL 1 : 10 diluted Matrigel for 20–30 min at 37 °C. Next, 300 µL of cell suspension was added on top of the filter units. Then, 500 µL of H14 medium with 10% FBS was added to the wells in the 24-well

plates below the filters. Finally, cells were incubated at 37 °C and 5% CO₂ for 48 h. Noninvasive cells on top of the filters were removed with cotton swabs, followed by fixation with paraformaldehyde (PFA, 3.7%, Sigma; 252549) and DAPI staining (1 : 5000; Sigma, D9542). Ten images per filter unit were taken by the EVOS[®] FL Auto Imaging System (10×; TFS), followed by the batch analysis of the images in Macro IMAGEJ 1.52p. For normalization of the different cell numbers in the filter units, cells were seeded into a 24-well plate along with the filter units and cultured and treated in the same way as cells in the filter units.

2.7. Statistical analysis and bioinformatics

All experiments performed in this study were in at least triplicates. The metabolomic analysis of the *UGDH* knock-down treatment was in six replicates. The proteomic data were processed in PERSEUS (version 1.6.14.0, data imputation based on normal distribution, width = 0.3, downshift = 1.8, permutation-based FDR < 0.05) [54] and R (version 4.0.0, the University of Auckland, New Zealand). Plots in this study were generated in R software. The statistical significance for all two-sample comparisons was based on the two-sided Student's *t*-test (Welsch, *P* < 0.05). Gene Ontology (GO) functional annotation was conducted in DAVID (DAVID Bioinformatics Resources 6.8) with default settings [55,56]. Reactome pathway analysis was performed with Reactome (Pathway browser version 3.7; Reactome database release: 75) with default settings [57]. Proteins with permutation-based FDR < 0.05 were used for the GO annotation and Reactome pathway analysis. Patient survival was plotted in KM plotter (kmplot.com) with basal breast cancer patients (split patients by autoselect best cut-off) [58]. The phosphoproteomic data were analysed in the INGENUITY PATHWAY ANALYSIS (IPA) (QIAGEN, Germantown, MD, USA, version from 2018) for pathway enrichment and PERSEUS for motif enrichment analysis.

All the R codes used for figure plotting in this study could be found on https://github.com/QiongW56/UGDH_Publication_2021.

3. Results

3.1. The proteomic differences based on cell-of-origin outweigh proteomic changes that accompany EMT

Three breast EMT cell models consisting of epithelial and mesenchymal breast cell line pairs were used in this

study (Fig. 1), namely, D492/D492M (D492 EMT model), HMLE/HMLEM (HMLE EMT model) and PMC42LA/PMC42ET (PMC42 EMT model). All three epithelial cell lines presented a typical cobblestone-shaped epithelial cell phenotype, while all the mesenchymal cells showed flattened mesenchymal morphology with undefined cell contour (Fig. S1B). The three EMT cell models presented different luminal/myoepithelial/basal phenotypes, with all three models possessing certain degrees of basal breast cell properties.

Irrespective of being epithelial or mesenchymal, cell lines of the same origin were grouped on the proteomic level (Fig. 2A). The PMC42 model shared the least similarities with the other EMT models (Fig. 2B). To confirm the epithelial and mesenchymal phenotypes on the molecular level, we quantified the EMT markers captured by the proteomic analysis from an EMT marker database [59]. VIM, LGALS1 and SERPINE1 were consistently upregulated in the mesenchymal cells, while PKP3 was downregulated (Fig. 2C–F). Not all EMT markers found in this study were, however, consistently altered among all three models, that is CD44, LMNB1, MSN, FLNA, TLN1, FSCN1, EGFR, S100A2 and NDRG1 (Fig. S2). Since E-cadherin (CDH1) and N-cadherin (CDH2), two typical EMT markers [60], were not covered in the proteomic analysis, we checked the expression of these by real-time PCR. CDH1 was significantly downregulated, while CDH2 was significantly upregulated in all EMT models (Fig. 2G,H).

3.2. Cell–cell and cell–extracellular matrix interactions are altered in EMT, and a diversity of pathways and molecular activities are changed in D492 as opposed to protein translation in HMLE and PMC42

Heterogeneity and plasticity are two intrinsic characteristics of EMT. To further define the epithelial and mesenchymal cells in all three EMT models, we compared their proteomes with respect to the number and profile of the significantly altered proteins along with their biological function and identified consistent EMT markers.

In total, 873 proteins were deemed valid proteins in identification and quantification (Table S3). In the D492 model, 188 out of the 873 valid proteins (21.5%) were significantly changed after EMT (permutation-based FDR < 0.05). In the HMLE model, 436 out of 873 proteins (49.9%) were significantly altered, while 200 proteins (22.9%) were significantly changed in the PMC42 model (Fig. 3A). Out of the significantly altered proteins, 55.9% (105/188) in the D492 model, 18.8% (82/436) in the HMLE model, while 63.5% (127/200) in the PMC42 model were upregulated after EMT

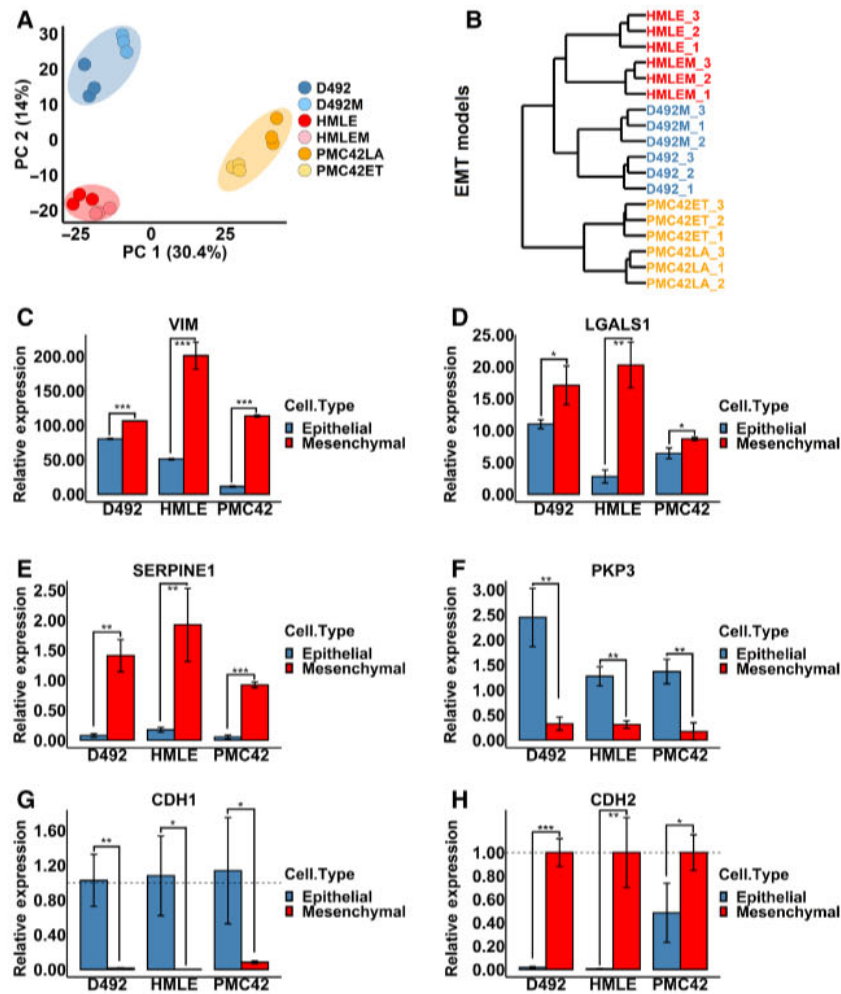


Fig. 2. EMT markers in the three breast EMT cell models. (A, B) Proteomic analysis of the three EMT models revealed cell lines with the same origin were more similar than their epithelial or mesenchymal states. The D492 EMT model was more similar to the HMLE model than the PMC42 model. Proteins with valid identification and quantification were included in the analysis (Table S3). Protein levels of the known EMT markers VIM (C), LGALS1 (D), SERPINE1 (E) and PKP3 (F) were consistently altered in all EMT models. RNA expression of CDH1 was downregulated (G), while RNA expression of CDH2 was upregulated after EMT (H). Student's *t*-test, **P* < 0.05; ***P* < 0.01; ****P* < 0.001; *n* = 3. The error bars indicate standard deviation. VIM, vimentin; LGALS1, galectin-1; SERPINE1, plasminogen activator inhibitor 1; PKP3, plakophilin-3; CDH1, E-cadherin; CDH2, N-cadherin.

(Fig. 3B). To ensure reproducibility of the proteomic data used in this study (Table S4), we compared the current proteomic data set with the previously generated data for the D492 EMT model [26]. The correlation coefficient of these two data sets was 0.936 (Fig. S3).

We next filtered the identified proteins based on their log₂ fold changes and $-\log_{10}$ *P*-values (Fig. 3C–E) and summarized the consistently altered proteins in all three EMT models (Fig. 3F and Table 1) to identify common changes in EMT. A literature search for each EMT target revealed that all had been associated with EMT previously, albeit to a different extent (Table 1). To evaluate these consistently altered EMT

confirmed the expression of these markers in the tumorigenic breast mesenchymal cell line D492HER2. All the targets detected in D492HER2 showed the same trends in changes (Table 1).

To define functional changes in EMT, we annotated the GO terms for the significantly changed proteins (Table S3) and observed that the Biological Process (BP) ‘cell–cell adhesion’ was altered in all three EMT models (Fig. 4A–C). The D492 model had the least similarity compared with the other two models, with only one common BP term (i.e. cell–cell adhesion) out of the top 10 enriched BP terms (Fig. 4A). In contrast, the PMC42 model shared its top seven terms with HMLE (Fig. 4B

We next filtered the identified proteins based on their log₂ fold changes and $-\log_{10}$ *P*-values (Fig. 3C–E) and summarized the consistently altered proteins in all three EMT models (Fig. 3F and Table 1) to identify common changes in EMT. A literature search for each EMT target revealed that all had been associated with EMT previously, albeit to a different extent (Table 1). To evaluate these consistently altered EMT markers in the context of cancer progression, we

examined the GO terms for the significantly changed proteins (Table S3) and observed that the Biological Process (BP) ‘cell–cell adhesion’ was altered in all three EMT models (Fig. 4A–C). The D492 model had the least similarity compared with the other two models, with only one common BP term (i.e. cell–cell adhesion) out of the top 10 enriched BP terms (Fig. 4A). In contrast, the PMC42 model shared its top seven terms with HMLE (Fig. 4B, C). The same trend was observed using enriched

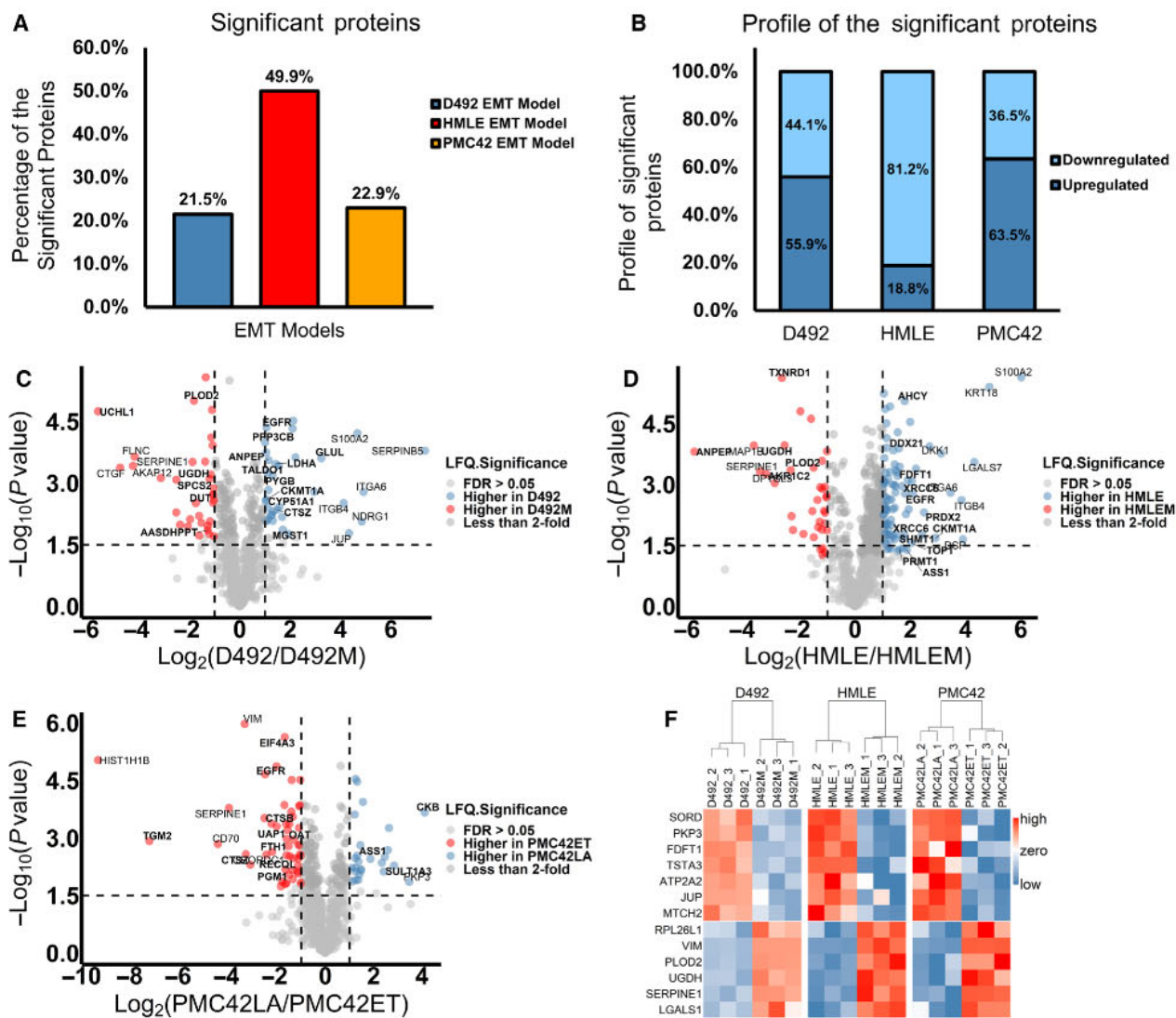


Fig. 3. Proteomic analysis of the three breast EMT cell models. (A) Percentages of significantly altered proteins in the EMT models (permutation-based FDR < 0.05). (B) Up- and downregulation profiles for all the significantly changed proteins in the EMT models. The log₂ (epithelial/mesenchymal ratio) along with the $-\log_{10}(P\text{-value})$ for each protein was plotted for the D492 model (C), HMLE model (D) and PMC42 model (E). Proteins with FDR (permutation-based) less than 0.05 and fold change more than 2 are coloured. The horizontal and vertical dashed lines indicate a P -value of 0.03 [$-\log_{10}(P\text{-value}) = 1.5$] and a 2-fold change, respectively. The annotated proteins had a log₂ (fold change) of more than 3. Proteins involved in metabolism with a log₂(fold change) of more than 1 for D492 model, 1.5 for HMLE and PMC42 models were bold label marked. $n = 3$. (F) A list of proteins significantly changed in the same direction (Student's t -test, $P < 0.05$) in all three EMT models. SERPINE1, RPL26L1, PLOD2, UGDH, LGALS1 and VIM were upregulated, while JUP, PKP3, MTCH2, ATP2A2, DFDT1, SORD and TSTA3 were downregulated after EMT.

Reactome pathway analysis (Fig. 4D–F). The altered Reactome pathways in the D492 model were related to response to cell stress, IGF signalling and interleukin-12 signalling (Fig. 4D). In both the HMLE and PMC42 models, changes were, however, mainly to pathways involved in the protein translational process (Fig. 4E,F). Comparison of changes to cellular components (Fig. S4A–C) and molecular function (Fig. S4D–F) was similarly indicative of more similarities in changes to

protein function following EMT in the HMLE and PMC42 models as compared to the D492 model.

3.3. UGDH is negatively correlated with patient survival and affects cell proliferation, cell invasion and SNAI1 expression

Next, we focused on the metabolic changes during EMT. Out of the thirteen identified targets listed in

Table 1. The EMT targets were significantly different (Student's *t*-test, $P < 0.05$) in all EMT models. The literature related to each target in terms of EMT was also listed. Changes in these targets in another breast mesenchymal cell line with tumorigenicity were consistent with the findings in this study.

Prot ID	Protein name	Gene name	Log2 (D492/D492M)	Log2 (HMLE/HMLEM)	Log2 (PMC42LA/PMC42ET)	-Log (P-value D492s)	-Log (P-value HMLEs)	-Log (P-value PMC42s)	EMT-related literature	Gene expression in mesenchymal cells with tumorigenicity (Log2 ratio)
121-1	Plasminogen activator inhibitor 1	SERPINE1	-4.236	-3.442	-3.993	3.416	3.313	3.780	[70,72,97]	-4.739
133-3	60S ribosomal protein L26-like 1	RPL26L1	-2.367	-1.123	-1.346	1.981	2.349	1.925	[98]	Not detected
1469-1	Procollagen-lysine, 2-oxoglutarate 5-dioxygenase 2	PLOD2	-1.817	-1.504	-1.121	5.005	3.411	2.072	[70,71]	-1.687
1701	UDP-glucose 6-dehydrogenase	UGDH	-1.193	-2.550	-0.779	3.101	3.962	2.285	[27,28,32,34,75]	-0.828
382	Galectin-1	LGALS1	-0.623	-2.912	-0.444	1.769	3.035	1.799	[67,69,70]	-0.422
670	Vimentin	VIM	-0.407	-1.979	-3.343	5.493	4.802	5.970	[4]	-0.957
1630	GDP-L-fucose synthase	TSTA3	0.553	1.009	0.508	2.871	2.517	1.789	[99,100]	0.562
1796	Sorbitol dehydrogenase	SORD	0.599	1.459	1.452	2.457	2.957	2.806	[101]	0.111
268	Squalene synthase	FDFT1	0.683	1.536	0.491	3.510	3.215	1.462	[102]	0.722
615	Sarcoplasmic/endoplasmic reticulum calcium ATPase 2	ATP2A2	0.919	0.523	0.641	2.388	1.551	2.316	[103]	0.299
1609	Mitochondrial carrier homolog 2	MTCH2	1.239	0.725	0.899	2.219	1.624	3.015	[99]	0.198
446	Plakophilin-3	PKP3	2.958	2.057	3.478	2.786	3.077	1.850	[66,68]	3.458
923	Junction plakoglobin	JUP	4.343	1.541	1.214	1.783	1.356	3.611	[104,105]	4.344

Table 1. The EMT targets were these targets in another breast r

UniProt ID	Protein name
P05121-1	Plasminogen activator inhibitor 60S ribosomal protein L26-like
Q9JUNX3	Procollagen-lysine 2-oxoglutarate 5-dioxygenase
O00469-1	UDP-glucose 6-dehydrogenase
O60701	Galectin-1
P09382	Vimentin
P08670	GDP-L-fucose synthase
Q13630	Sorbitol dehydrogenase
Q00796	Squalene synthase
P37268	Sarcoplasmic/endoplasmic reticulum calcium ATPase 2
P16615	Mitochondrial cytochrome c homolog 2
Q9Y6C9	Plakophilin-3
Q9Y446	Junction plakoglobin
P14923	

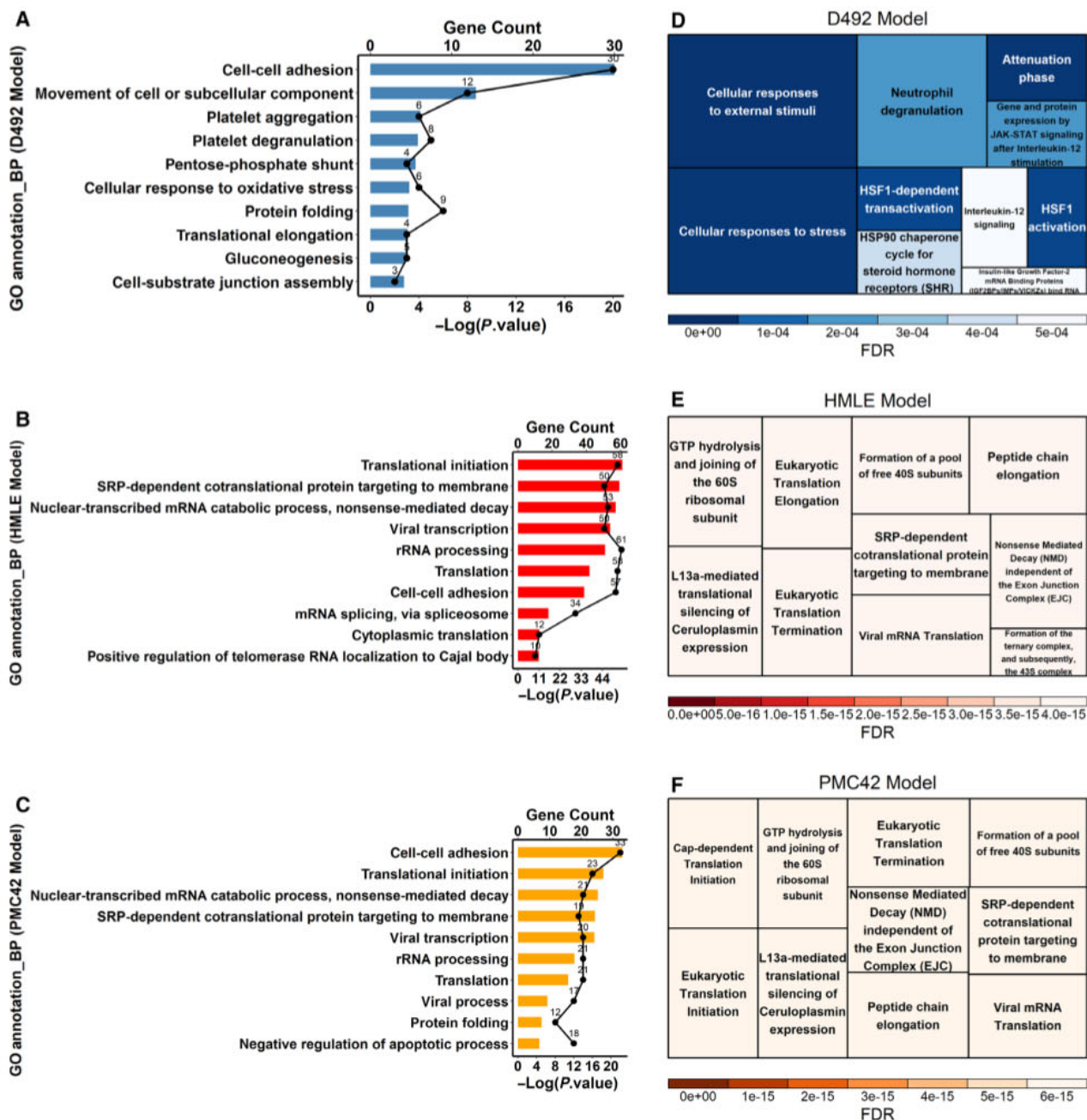


Fig. 4. Functional annotation of the GO terms (BP) and Reactome pathway analysis for the three EMT models. (A–C) Functional annotation of the GO terms (BP) was conducted on the DAVID platform (DAVID Bioinformatics Resources 6.8) for the D492 model (A), HMLE model (B), and PMC42 model (C). The GO terms were listed according to the $-\log_{10} P$ -value in descending order. The numbers of genes in each GO term were also plotted as dots/line plots. (D–F) Reactome pathway analysis (Pathway browser version 3.7; Reactome database release: 75) for the D492 model (D), HMLE model (E) and PMC42 model (F). Data used for both the GO annotation and the pathway analysis (Table S3) were proteins significantly different in each EMT model (permutation-based FDR < 0.05). Default settings in the DAVID and Reactome platforms were used. BP, biological process.

Table 1, four proteins were involved in metabolism: FDFT1, SORD and TSTA3 were downregulated while UGDH was upregulated (Fig. 5A–D). We further tested the RNA expression of UGDH, which showed

the most changes to protein expression in all EMT models and was associated with cancer aggressiveness. Though there was no significance in the D492 and PMC42 models, the upregulating trends in all EMT

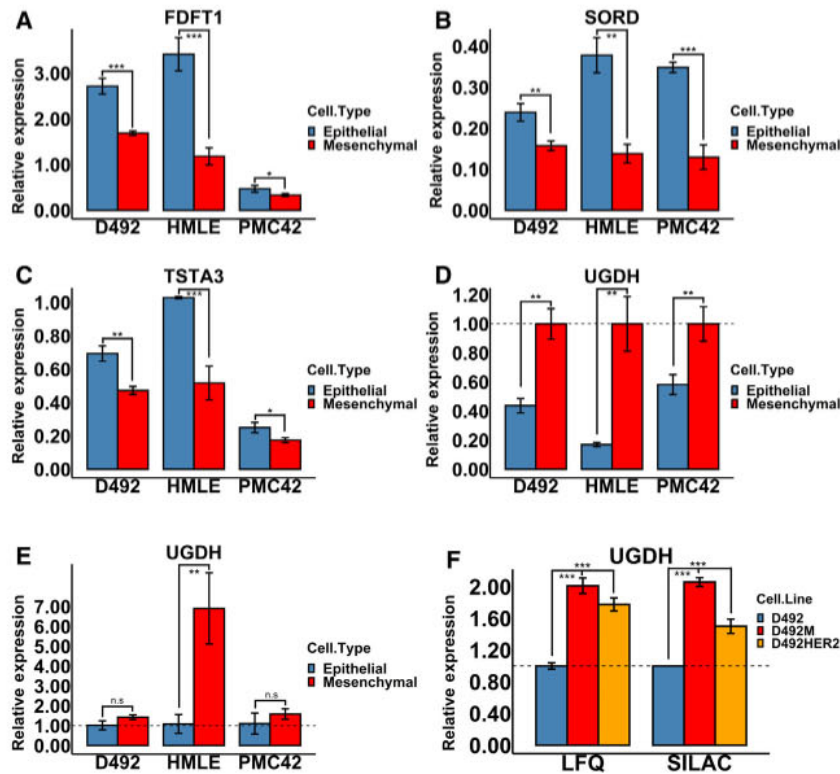


Fig. 5. Four metabolic enzymes changed consistently in all EMT models. (A–D) The proteomic analyses revealed that the metabolic enzymes FDFT1, SORD, TSTA3 and UGDH changed consistently in all EMT models. (E) The RNA level of UGDH in all EMT models was consistently higher in the mesenchymal cell lines. (F) The UGDH protein level in the epithelial and mesenchymal cells was confirmed in another data set [26] and further confirmed in another tumorigenic breast mesenchymal cell line D492HER2. Student's *t*-test, **P* < 0.05; ***P* < 0.01; ****P* < 0.001; *n* = 3. The error bars indicate standard deviation. FDFT1, squalene synthase; SORD, sorbitol dehydrogenase; TSTA3, GDP-L-fucose synthase; UGDH, UDP-glucose 6-dehydrogenase.

models were seen (Fig. 5E). To relate these findings to breast cancer, we tested the protein level of UGDH in the tumorigenic breast mesenchymal cell line D492HER2. UGDH was upregulated in D492HER2 as observed in nontumorigenic mesenchymal cell line D492M (Fig. 5F).

Recent studies have reported that UGDH affects patient survival [34], cell proliferation [32,37], cell invasion [27], cell migration [34,37] and SNAIL1 expression [28]. We set out to confirm these effects of UGDH in our EMT cell lines. High UGDH level was associated with worse patient survival in basal breast cancer patients based on KM plotter (Fig. 6A). Based on this, we analysed effects of UGDH on cell morphology, proliferation, invasion and SNAIL1 expression in two types of breast mesenchymal cells: nontumorigenic D492M and tumorigenic D492HER2 via siRNA-mediated knock-down of *UGDH* (Fig. S5). Knock-down of *UGDH* did not yield observable morphological changes but slowed down cell growth (Fig. 6B,C) and

SNAIL1 RNA expression was downregulated after *UGDH* knock-down, which was also consistent with the literature (Fig. 6F,G and Fig. S6D,E).

3.4. GPC is downregulated while NAA is upregulated following *UGDH* knock-down in the mesenchymal cells

UGDH catalyses the conversion of UDP-Glc to UDP-GlcA that are constituents of glycosaminoglycans and N- and O-linked glycans [61]. To confirm the metabolic impacts of UGDH in mesenchymal cells, we knocked down *UGDH* with siRNAs and performed metabolomic analysis in all three mesenchymal cell lines. Samples from the same cell line clustered together at the metabolic level despite *UGDH* knock-down (Fig. 7A,B). As with the proteome, the metabolome of D492M was closer to that of HMLEM than the metabolome of PMC42ET. Knock-down of *UGDH* did not confer a distinct metabolic phenotype com-

patients based on KM plotter (Fig. 6A). Based on this, we analysed effects of UGDH on cell morphology, proliferation, invasion and SNAI1 expression in two types of breast mesenchymal cells: nontumorigenic D492M and tumorigenic D492HER2 via siRNA-mediated knock-down of *UGDH* (Fig. S5). Knock-down of *UGDH* did not yield observable morphological changes but slowed down cell growth (Fig. 6B,C) and invasion (Fig. 6D,E and Fig. S6A–C) in both cell lines.

knocked down *UGDH* with siRNAs and performed metabolomic analysis in all three mesenchymal cell lines. Samples from the same cell line clustered together at the metabolic level despite *UGDH* knock-down (Fig. 7A,B). As with the proteome, the metabolome of D492M was closer to that of HMLEM than the metabolome of PMC42ET. Knock-down of *UGDH* did not confer a distinct metabolic phenotype compared with the scramble control in any of the

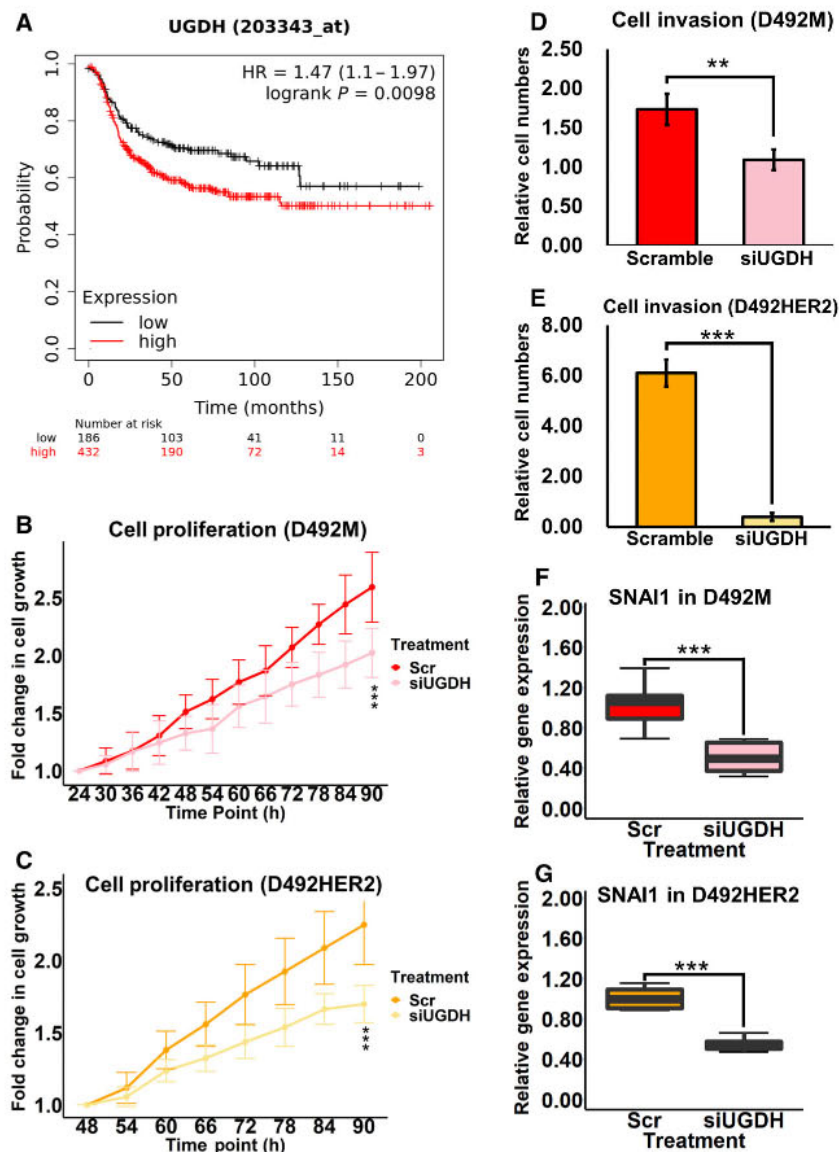


Fig. 6. Functional analysis of UGDH in EMT. (A) The Kaplan–Meier plot of UGDH in basal breast cancer patients was downloaded from kmpplot.com. (B, C) Cell proliferation slowed down with the siRNA knock-down of *UGDH* in both nontumorigenic D492M (B) and tumorigenic D492HER2 (C). n equals 4, and three spots were chosen for each replicate during the imaging process. (D, E) Cell invasion decreased with *UGDH* knock-down in both nontumorigenic D492M (D) and tumorigenic D492HER2 (E). n equals 3, and 10 spots were chosen for each replicate during the cell counting process. (F, G) One of the main EMT transcription factors SNAI1 was downregulated after the siRNA knock-down of *UGDH* in both nontumorigenic D492M ($n = 7$) (F) and tumorigenic D492HER2 ($n = 4$) (G). Student's t -test, $**P < 0.01$; $***P < 0.001$. The error bars indicate standard deviation. SNAI1, Snail family transcriptional repressor 1; UGDH, UDP-glucose 6-dehydrogenase.

mesenchymal cell lines (Fig. 7B). An increasing trend of UDP-Glc was observed in all the mesenchymal cell lines with all the siUGDH treatments, although non-significant for one of the siRNAs (Fig. 7C). UDP-GlcA decreased in all the mesenchymal cell lines in all the siUGDH treatments, although nonsignificantly with one siRNA in D492M (Fig. 7D).

To better evaluate the systemic changes of UGDH on metabolism, we carried out an untargeted metabolomics analysis. Knocking down *UGDH* significantly decreased the intracellular glycerophosphocholine (GPC) level and increased acetylaspartate (NAA) in all the mesenchymal cell lines (Fig. 7E,F), which was confirmed in the aggressive D492HER2 and MDA-

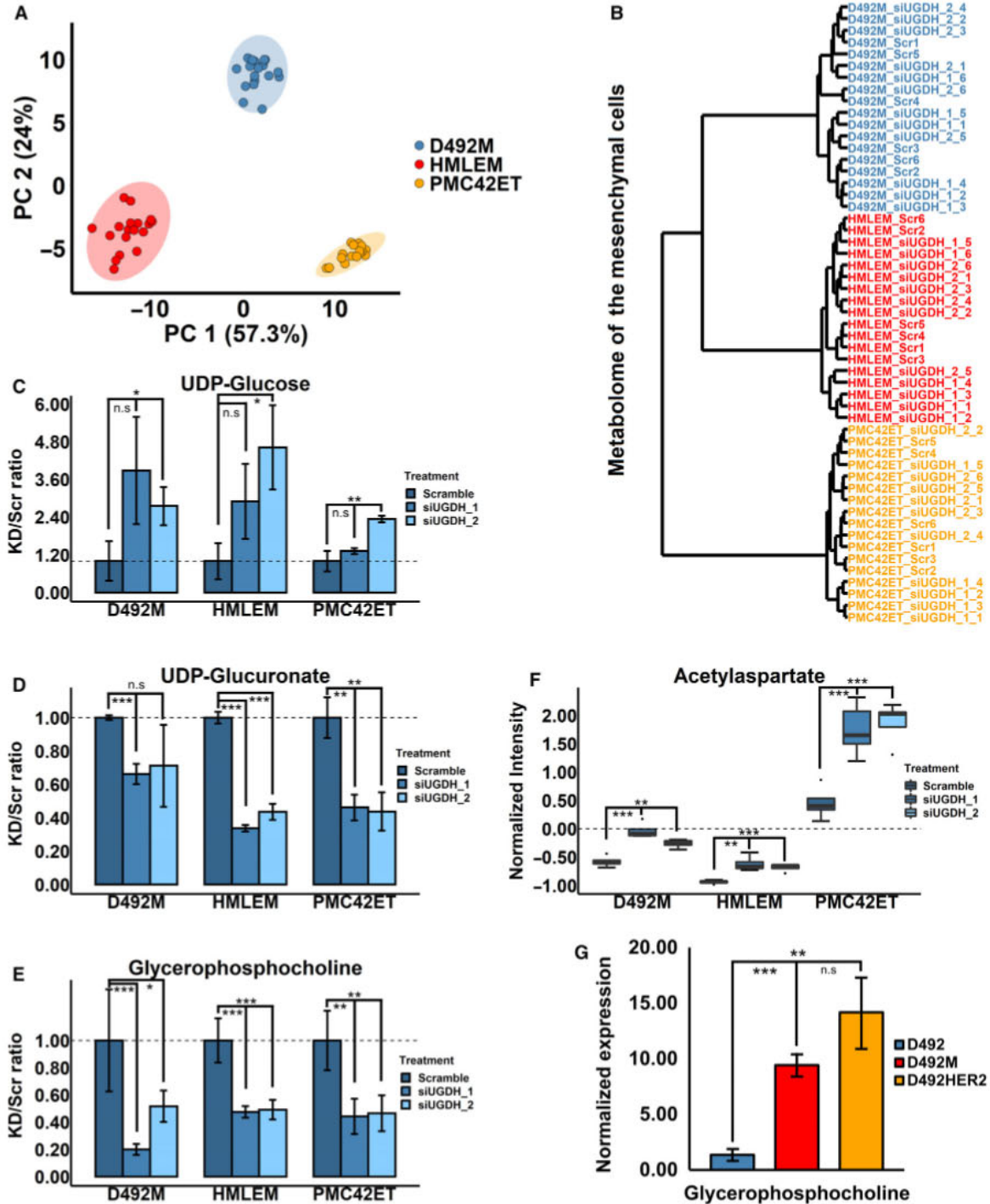


Fig. 7. Metabolomic changes after siRNA knock-down of *UGDH* in the mesenchymal cell lines. (A, B) Metabolomic clustering of the mesenchymal cell lines with different treatments. Valid metabolite identification and quantification from the negative, positive and basic modes were integrated into the analysis. Samples clustered together based on the differences of their metabolome among different EMT models (A), and the D492 mesenchymal cells were closer to the HMLE mesenchymal cells than PMC42 at the metabolic level (B). (C) The *UGDH* substrate UDP-glucose was increased following siRNA knock-down of *UGDH* in all cell lines with two siRNAs ($n = 3$). (D) The *UGDH* product UDP-glucuronate was decreased with siRNA knock-down of *UGDH* in all the cell lines with two siRNAs ($n = 3$). (E, F) siRNA knock-down of *UGDH* significantly decreased GPC ($n = 5$) and increased acetylaspertate ($n = 4$) in all the cell lines with two siRNA treatments. (G) GPC level was higher in the nontumorigenic D492M than the epithelial D492, and it was the highest in the tumorigenic mesenchymal D492HER2 ($n = 3$).

Fig. 7. Metabolomic changes after siRNA knock-down of *UGDH* in the mesenchymal cell lines. (A, B) Metabolomic clustering of the mesenchymal cell lines with different treatments. Valid metabolite identification and quantification from the negative, positive and basic modes were integrated into the analysis. Samples clustered together based on the differences of their metabolome among different EMT models (A), and the D492 mesenchymal cells were closer to the HMLE mesenchymal cells than PMC42 at the metabolic level (B). (C) The *UGDH* substrate UDP-glucose was increased following siRNA knock-down of *UGDH* in all cell lines with two siRNAs ($n = 3$). (D) The *UGDH* product UDP-glucuronate was decreased with siRNA knock-down of *UGDH* in all the cell lines with two siRNAs ($n = 3$). (E, F) siRNA knock-down of *UGDH* significantly decreased GPC ($n = 5$) and increased acetylaspartate ($n = 4$) in all the cell lines with two siRNA treatments. (G) GPC level was higher in the nontumorigenic D492M than the epithelial D492, and it was the highest in the tumorigenic mesenchymal D492HER2 ($n = 3$). Student's *t*-test, * $P < 0.05$; ** $P < 0.01$; *** $P < 0.001$. The error bars indicate standard deviation. *UGDH*, UDP-glucose 6-dehydrogenase.

MB-231 cell lines (Fig. S7A–D). To investigate whether GPC and NAA were associated with the UGDH level and differently expressed regardless of tumorigenicity, we tested the GPC and NAA levels in the epithelial D492, nontumorigenic mesenchymal D492M and tumorigenic mesenchymal D492HER2 cells. GPC was higher in both D492M and D492HER2 compared with D492 (Fig. 7G). We further looked into the connection between GPC and the mesenchymal state based on published data sets in the literature [62,63] but did not observe any significant correlation (Fig. S7E and Table S5). siRNA-mediated knock-down of *UGDH* did not yield significant and consistent changes to choline and phosphocholine (Fig. S7F,G).

Glycerophosphocholine is part of the choline synthetic pathway from phosphatidylcholine (PtdCho), and NAA is closely associated with acetyl-CoA and central carbon metabolism. To query how changes to UDP-GlcA might relate to GPC and NAA processing via changes in metabolic flux, we performed *in silico* knock-down of *UGDH* using tailored genome-scale metabolic models of D492 [23,25]. Changes to metabolic flux were observed within keratan metabolism, hyaluronan processing, pentose phosphate pathway and the central carbon metabolic pathways (Table S6). Negligible changes were, however, observed to GPC production and consumption.

3.5. PDGFRB signalling regulates UGDH potentially via NFκB-p65

We next investigated the upstream regulation of UGDH by analysing the secretome of the D492 model [64]. IGF, TGF-β and PDGFD signalling regulators were highly presented in the culture medium of D492M cells (Fig. 8A). PDGFRB was highly expressed in the nontumorigenic D492M (Fig. 8B) and the tumorigenic D492HER2 mesenchymal cell lines (Fig. S8A) [65], and PDGFD was secreted by D492M (Fig. 8C). We thus focused on the role of PDGF

signalling in UGDH regulation. In addition, the motif enrichment analysis of the phosphorylation sites within the phosphoproteomic data (Table S7) revealed potentially altered kinases in the D492 EMT model, including the downstream target of the PDGF signalling PKC kinase (Fig. 8D). siRNA-mediated knock-down of *PDGFRB* decreased both the PDGFR signalling downstream regulator *RELA* (NFκB-p65) and UGDH in D492M (Fig. 8E–G) and D492HER2 (Fig. S8B–D). We further investigated the impact of *RELA* on UGDH and found that siRNA-mediated knock-down of *RELA* decreased the UGDH RNA level in D492M (Fig. 8H,I and Fig. S8E,F). We observed the same effect of *RELA* knock-down on UGDH in D492HER2 with only one siRNA (Fig. S8G–J).

4. Discussion

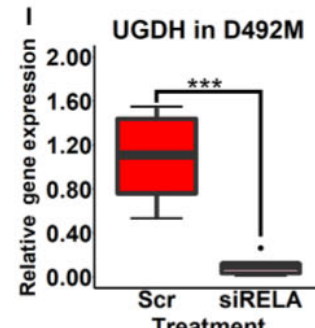
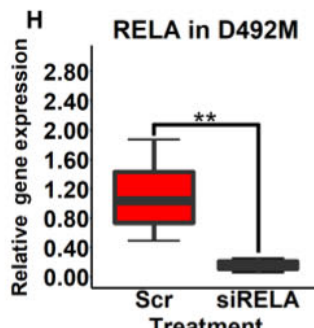
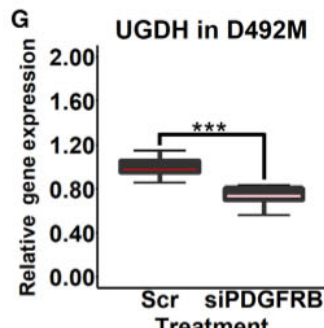
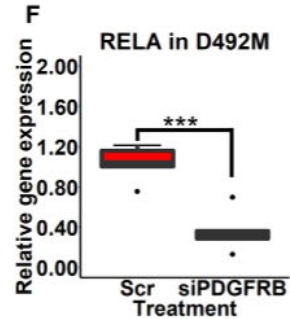
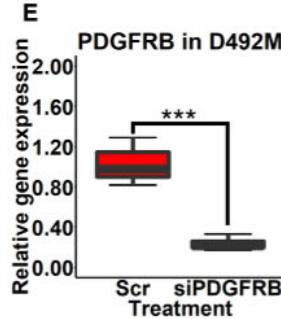
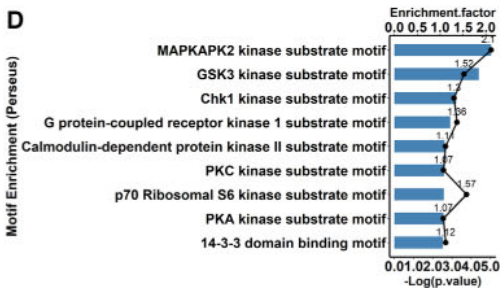
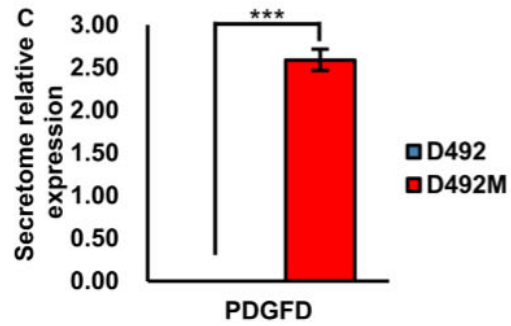
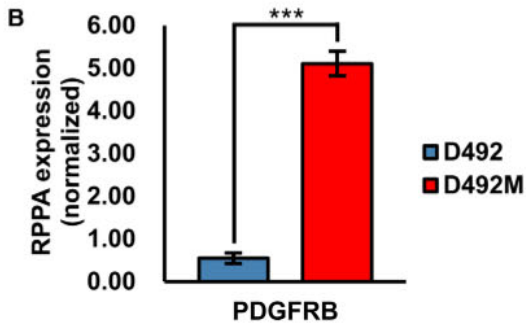
Herein we set out to determine common metabolic changes in cell models used to study EMT in breast epithelium. We chose the D492, HMLE and PMC42 EMT cell models on account of the spontaneous EMT induction approaches and the nontumorigenic properties of these cell lines to ensure the intrinsic characteristics and plasticity of EMT (Fig. 1). First, we validated and compared the EMT cell models on the proteomic level (Fig. 2A,B). Cell lines clustered based on their origin instead of their epithelial or mesenchymal characteristics, indicating that the spontaneous epithelial–mesenchymal switches during EMT/MET are subtle compared with the imprinted intrinsic genetic differences among these cell models.

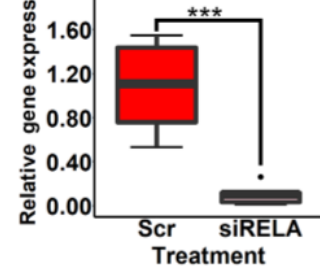
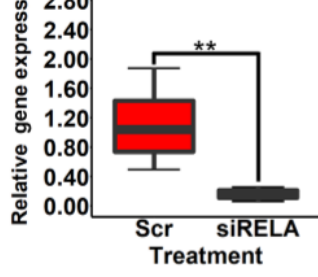
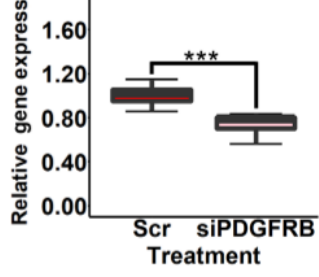
VIM, LGALS1, SERPINE1, PKP3 and the CDH1-CDH2 switch were consistently altered in all the EMT models (Fig. 2C–H) and have all been related to EMT in different cancer types [4,60,66–72]. Vimentin, a type III intermediate filament and well-known EMT marker, shapes the cell structure and modifies cell movements and cell adhesion [73]. SERPINE1, a key player in endothelial homeostasis, is highly upregulated in EMT. However, the function of SERPINE 1 in EMT

Fig. 8. PDGFRB regulates UGDH via *RELA* (NFκB-p65) in D492M. (A) Top differently secreted growth factors from the secretome of the D492 EMT model were reported (permutation-based FDR < 0.05). (B) PDGFRB was highly expressed in mesenchymal cells than epithelial cells in the D492 model on the protein level based on the RPPA analysis ($n = 3$) [65]. (C) PDGFD protein was highly secreted in mesenchymal cells than epithelial cells in the D492 model ($n = 3$). (D) Motif enrichment of the phospho-proteome in the D492 EMT model suggested that PKC kinase activity, among others, was highly enriched in EMT. Enrichment factors ≥ 2 ; motif enrichment terms were ranked based on the $-\log_{10}(P\text{-value})$. (E) The knock-down efficiency of *PDGFRB* with siRNA in the D492M cell line was around 80% ($n = 7$). (F) *RELA* (NFκB-p65) was downregulated after the siRNA knock-down of *PDGFRB* in D492M ($n = 5$). (G) UGDH was downregulated after the siRNA knock-down of *PDGFRB* in D492M ($n = 7$). (H) The knock-down efficiency of *RELA* with the first siRNA in D492M was about 80% ($n = 6$). (I) UGDH was downregulated after the siRNA knock-down of *RELA* in D492M with the first siRNA ($n = 6$). Student's *t*-test, $**P < 0.01$; $***P < 0.001$. The error bars indicate standard deviation. PDGFRB, platelet-derived growth factor receptor beta; *RELA* (NFκB-p65), nuclear factor NF-kappa-B p65 subunit; UGDH, UDP-glucose 6-dehydrogenase.

A

Protein ID	Protein Name	Gene Name	-Log(P value)	FDR	-Log2(D492/D492M)
Q8WX77	Insulin-like growth factor-binding protein-like 1	IGFBPL1	2.633	0.004	-6.055
P22692	Insulin-like growth factor-binding protein 4	IGFBP4	6.401	0.000	-5.008
P61812	Transforming growth factor beta-2	TGFB2	4.302	0.000	-4.524
P01137	Transforming growth factor beta-1	TGFB1	1.773	0.014	-3.392
Q16270	Insulin-like growth factor-binding protein 7	IGFBP7	5.191	0.000	-3.341
Q9GZP0	Platelet-derived growth factor D	PDGFD	4.127	0.000	-3.273
P18065	Insulin-like growth factor-binding protein 2	IGFBP2	2.878	0.003	-1.729
Q15582	Transforming growth factor-beta-induced protein ig-h3	TGFB1	2.606	0.004	-0.967
M0QXF7	Myeloid-derived growth factor (Fragment)	MYDGF	3.098	0.002	-0.848
G3V3X5	Latent-transforming growth factor beta-binding protein 2	LTBP2	2.411	0.005	-0.750
J3KT38	Growth factor receptor-bound protein 2 (Fragment)	GRB2	1.933	0.013	-0.295
H7BYW6	Platelet-derived growth factor subunit A (Fragment)	PDGFA	1.646	0.019	0.505
P08581	Hepatocyte growth factor receptor	MET	1.478	0.024	0.610
P51858	Hepatoma-derived growth factor	HDGF	1.829	0.014	0.647
A0A0C4DH07	Latent-transforming growth factor beta-binding protein 4	LTBP4	2.645	0.004	0.827
P24592	Insulin-like growth factor-binding protein 6	IGFBP6	2.810	0.003	1.728
Q9H6S3	Epidermal growth factor receptor kinase substrate 8-like protein 2	EPS8L2	3.919	0.000	1.835
P00533	Epidermal growth factor receptor	EGFR	2.168	0.010	2.485
C9JD84	Latent-transforming growth factor beta-binding protein 1	LTBP1	4.083	0.000	2.501
Q14512	Fibroblast growth factor-binding protein 1	FGFBP1	6.742	0.000	8.075





is poorly understood. The possible role of SERPINE1 in EMT is to affect the function of urokinase-type plasminogen activator receptor (uPAR) to regulate extracellular matrix degradation [72]. LGALS1 is a carbohydrate-binding protein. One study shows that upregulation of LGALS1 decreases CDH1 and increases SNAI1 [67]. PKP3 is an epithelial marker and is under the control of the EMT transcriptional regulator ZEB1 [66,68]. All these EMT markers were consistently altered in the three EMT models (Fig. 2C–F). However, inconsistencies in EMT markers were also observed indicative of their different roles in EMT with respect to cell type. The PMC42 model was different from the other EMT cell models (Fig. S2), potentially reflecting the cell heterogeneity and partially expressed mesenchymal marker CDH2 in the epithelial cells (Fig. 2H) [74]. The consistently altered EMT markers were also confirmed in the tumorigenic breast mesenchymal cell line D492HER2 (Fig. 3F and Table 1), indicating that these markers are not only crucial for EMT but also potentially involved in tumorigenicity and malignancy, even though they are not critical for tumour initiation. Moreover, many of the consistently altered proteins identified in this study remain unexplored in the context of EMT (Table 1).

Our findings confirmed that changes to cellular morphology, cell–cell communication and cell–extracellular matrix interaction are among the main characteristics of EMT (Fig. 4 and Fig. S4). Even though the proteomes of the D492 cell lines were closer to HMLE (Fig. 2B), they shared the least similarity in the altered pathways post-EMT. The changed translational activities in HMLE and PMC42 and the altered responses to stress and signalling regulation in D492 suggest that in HMLE and PMC42, the epithelial or mesenchymal switch may largely be mediated by altered expression of proteins involved, whereas in D492, post-translational control of existing proteins may play a more important role. This may also reflect the more stem-like properties of the D492 epithelial cells that confer cell flexibility. Our findings indicate that distinct and dominant cell properties (e.g. stem cell properties) outweigh similar genetic backgrounds for EMT induction, while cells with disparate genetic backgrounds can rely on similar machineries to induce EMT.

Recently, a growing number of studies have focused on UGDH in cancer, and the roles of UGDH in tumour growth, metastasis and patient survival have been well documented [27,32,34–37]. Additionally, UGDH has been connected to EMT [27,28,32,34,75]. Arnold *et al.* [27] reported that UGDH was highly expressed in mesenchymal cells and mesenchymal-like

breast cancers and connected UDP-GlcA (the enzymatic product of UGDH) to extracellular matrix remodelling and mesenchymal-like properties. Furthermore, UGDH regulates SNAI1, a well-known EMT transcription factor, via UDP-Glc (the enzymatic substrate of UGDH) [28]. We confirmed the upregulation of UGDH in both nontumorigenic and tumorigenic mesenchymal cell lines, suggesting UGDH is associated with the mesenchymal feature in tumorigenic cell lines (Fig. 5F). Interestingly, even though the high expression of UGDH was associated with worse survival in basal breast cancer patients (Fig. 6A) and decreased UGDH jeopardized cell proliferation (Fig. 6B,C) and invasion (Fig. 6D,E and Fig. S6A–C), all the mesenchymal cells in this study possess upregulated UGDH and are nontumorigenic. Thus, elevated UGDH expression is likely not a trigger for tumour initiation, but tumorigenic cells may rely on UGDH to facilitate tumorigenicity and malignancy. UGDH may induce resistance to chemotherapy via drug elimination. This was supported by a recent study demonstrating that high levels of UGDH are correlated with worse prognosis in triple-negative breast cancer patients receiving chemotherapy, likely by promoting UDP-GlcA-mediated detoxification and elimination of epirubicin [76]. The effect of UGDH on SNAI1 supports that UGDH has a regulatory role in EMT and that its function may exceed its catalytic role, perhaps via nonconventional signalling regulatory effects such as glycosylation (Fig. 6F,G and Fig. S6D,E).

The D492 EMT model metabolome was more similar to HMLE than PMC42 (Fig. 7A,B), consistent with the proteomic analysis (Fig. 2A,B). In agreement with the literature, knock-down of *UGDH* increased UDP-Glc and decreased UDP-GlcA (Fig. 7C,D), both of which are important metabolites with wide impact on cells [27,28]. The most prominently altered metabolite was, however, GPC (Fig. 7E). Increased GPC in tumours indicates changes to choline metabolism, which has emerged as a hallmark of cancer progression [77]. GPC is negatively correlated with patient survival [78] and is high in basal-like breast cancer xenograft and oestrogen receptor-negative breast cancer patients [79,80]. Reduced GPC levels after chemotherapies are associated with better survival in breast cancer patients [78]. D492 and D492M are basal-like breast cell lines, while D492HER2, deemed as HER2-positive breast cell line, is more closely associated with the aggressive claudin low than other breast cancer types [26,81]. Claudin low is not a distinct intrinsic tumour subtype but may permeate various breast cancer types including HER2-positive [82]. The higher levels of GPC along with UGDH in

basal-like mesenchymal D492M and claudin-low D492HER2 are in congruence with the clinical observations. GPC may be involved in EMT, but the connection between GPC and EMT in cancer is unclear [83,84]. Li and colleagues detected GPC in 928 cell lines and performed different types of metabolite-gene association analyses. They reported various genes associated with GPC where the EMT master regulator TWIST1 was one of the top hits [62]. The insignificant correlation between GPC and mesenchymal cells (Fig. S7E) suggests that the increased GPC levels observed in the D492 mesenchymal cells are results of one or several regulators independent of mesenchymal traits. Our results support that GPC in part is regulated by the mesenchymal metabolic enzyme UGDH, but the molecular mechanisms underlying this warrant further investigation. *In silico* knock-down of *UGDH* in the genome-scale metabolic models revealed several metabolic changes (Table S6) primarily on account of rerouting of glucose flux away from UDP-GlcA formation and into glycolysis and associated pathways (e.g. PPP and TCA), which may be partially responsible for the increased NAA (Fig. 7F). It, however, imparted no changes in GPC, implying that the changes to metabolic fluxes encircling GPC due to a mass-action effect of UGDH are likely secondary to changes that arise through altered glycosylation. Cell osmotic pressure balance is vital for normal cell functions and cell survival. GPC is a well-known intracellular osmotic regulator, and proteoglycans serve as extracellular osmolytes [85]. The decreased intracellular GPC may thus counterbalance the decreased extracellular osmotic pressure induced by the reduced proteoglycans caused by the knock-down of *UGDH*.

Recently, studies have shown that UGDH regulates signalling factors and lipid metabolic genes, such as SNAI1-, SIP-1-, ERK/MAPK-, SIX1- and PPAR γ -targeted genes [27,28,32,34]. PPAR γ is a nuclear transcription factor regulating genes linked to lipid metabolism [86,87] that interacts with choline/PtdCho metabolism [88]. UGDH has been proposed to inhibit PPAR signalling and affect lipid metabolism [27]. Consistent with this, we observed a negative association between UGDH expression and PPAR γ signalling (Fig. S7H), suggesting the *UGDH* knock-down decreases intracellular GPC level via PPAR γ . Moreover, phospholipase A2 group XV (PLA2G15), which belongs to Cytosolic phospholipase A2 (cPLA2), is an enzyme catalysing the hydrolysis of phospholipids, potentially involved in the formation of GPC from PtdCho, and is under the control of ERK signalling [89,90]. Knock-down of *UGDH* has been reported to

highly invasive ovarian cancer cells [32]. We observed that both GPC and PLA2G15 were higher in the mesenchymal cell lines D492M and D492HER2 (Fig. 7G and Fig. S7I), implying UGDH may regulate GPC via pERK-PLA2G15. Taken together, UGDH may indirectly affect GPC via signalling regulations and/or lipid metabolism to retain the osmotic balance across the cell membrane, although further investigations are needed. Furthermore, the absence of UGDH in the list of genes associated with GPC reported in the literature indicates UGDH may not be a dominant GPC regulator [62].

Slit2, SP1, TGF- β , hypoxia, p38^{MAPK}, LMP2A and PI3K/Akt affect and/or regulate UGDH expression, which highlights that UGDH is under complex regulation network control [29–31,33]. These regulators are potentially mediated by PDGF signalling that, along with the downstream transcription factor NF κ B, is dysregulated in cancer progression and EMT [7,91,92]. Tam *et al.* [7] reported a switch from EGFR to PDGFR signalling in cancer stem cell formation and EMT. The higher expression of PDGFRB and secretion of PDGFD in D492M compared with D492 suggest PDGFRB signalling is upregulated in mesenchymal cells (Fig. 8A–C and Fig. S8A) supported by the increased phospholipase C, PI3K/Akt and PKC α signalling (Fig. S7H and Fig. 8D) since these are well-known downstream targets of PDGFR [7,93]. This is consistent with PDGFD-PDGFRB signal regulation of EMT [94,95]. NF κ B-p65 is a downstream regulator of PDGFR signalling [92,96]. Downregulating either *PDGFRB* or *NF κ B-p65* decreased UGDH expression on the RNA level in both D492M and D492HER2. However, the impacts of PDGFRB and NF κ B-p65 on UGDH were dampened in D492HER2 compared with D492M (Fig. 8E–I and Fig. S8B–J). We have previously noticed that D492HER2 is a less complete mesenchymal cell line than D492M, suggesting that the regulations of PDGFRB and NF κ B-p65 on UGDH are more dominant in complete mesenchymal cells [26]. It thus appears that UGDH is part of an interactive signalling and metabolic network in which PDGFRB differently regulates UGDH via NF κ B-p65 depending on specific cell types.

5. Conclusions

In conclusion, we used three breast EMT cell models to study proteomic changes in EMT, focusing on metabolic reprogramming. We further studied the downstream functions of the metabolic enzyme UGDH in cancer progression and metabolism, and finally, we explored the upstream signalling regulating

(Fig. S7H), suggesting the *UGDH* knock-down decreases intracellular GPC level via PPAR γ . Moreover, phospholipase A2 group XV (PLA2G15), which belongs to Cytosolic phospholipase A2 (cPLA2), is an enzyme catalysing the hydrolysis of phospholipids, potentially involved in the formation of GPC from PtdCho, and is under the control of ERK signalling [89,90]. Knock-down of *UGDH* has been reported to downregulate the phosphorylation of ERK (pERK) in

5. Conclusions

In conclusion, we used three breast EMT cell models to study proteomic changes in EMT, focusing on metabolic reprogramming. We further studied the downstream functions of the metabolic enzyme UGDH in cancer progression and metabolism, and finally, we explored the upstream signalling regulating UGDH (Fig. 9). Several proteins were found to be

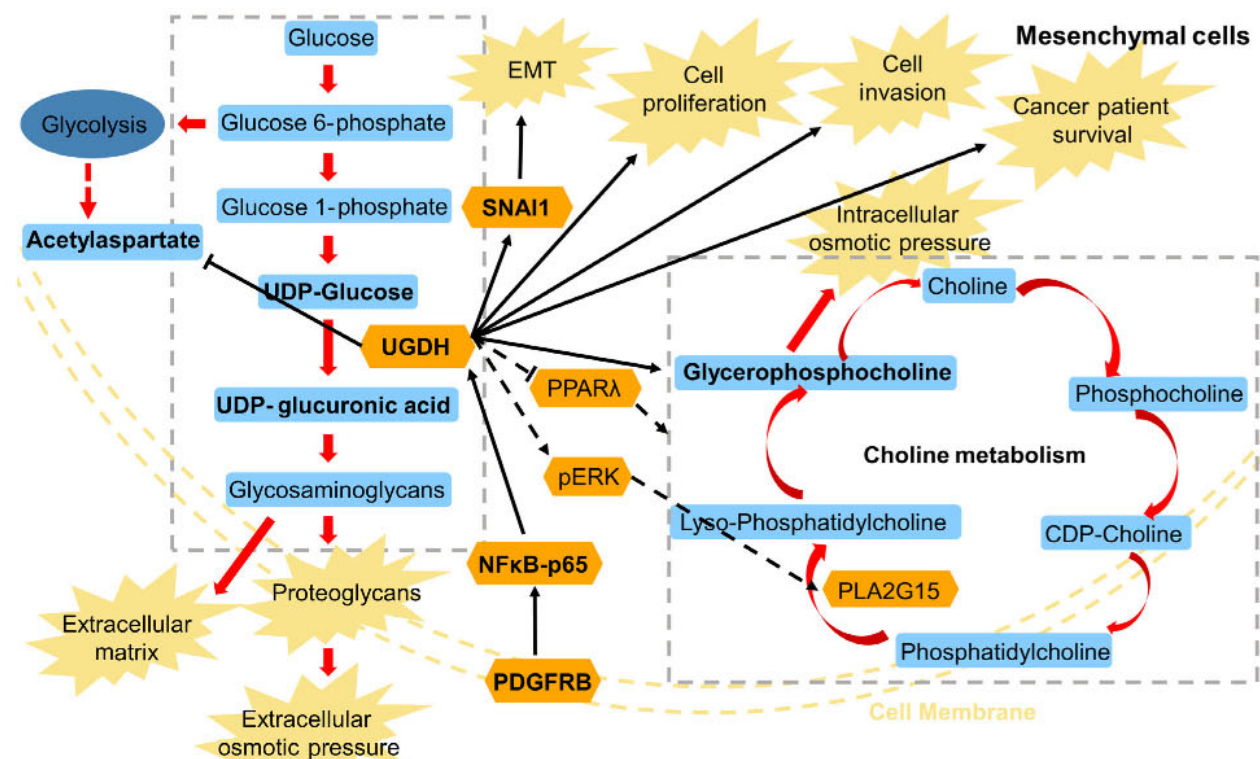


Fig. 9. Summary of the study. This figure illustrates the main metabolic pathways and findings involved in this study. UGDH catalyses UDP-glucose into UDP-glucuronic acid, an indispensable unit for glycosaminoglycans, proteoglycans and extracellular matrix. In this study, UGDH was found to be highly expressed in the mesenchymal cells and affect cancer patient survival, mesenchymal cell proliferation and invasion and the EMT transcription factor SNAI1, and it was under the control of the PDGFRB-NFκB pathway. In addition, the knock-down of *UGDH* with siRNAs significantly decreased the intracellular GPC levels and increased the acetylaspartate (NAA) levels in all the mesenchymal cell lines. NAA is closely linked to the central carbon metabolism and potentially affected by the mass-action effects of *UGDH* knock-down. GPC is an intracellular osmolyte and part of the choline metabolism. Knock-down of *UGDH* hindered the formation of proteoglycans and further decreased the extracellular osmotic pressure, which could be counteracted by the reduced intracellular osmotic pressure induced by GPC. Based on the literature, we hypothesized that to ease the osmotic stress, knock-down of *UGDH* affected PPAR γ -lipid metabolism and/or pERK-PLA2G15 to regulate GPC. However, further studies are needed to address this question. UGDH, UDP-glucose 6-dehydrogenase; SNAI1, Snail family transcriptional repressor 1; PDGFRB, platelet-derived growth factor receptor beta; NFκB-p65, nuclear factor NF-kappa-B p65 subunit; PPAR γ , peroxisome proliferator-activated receptor γ ; pERK, phosphorylated extracellular signal-regulated kinase; PLA2G15, phospholipase A2 group XV.

involved in the EMT programme and likely to participate in normal human breast gland development, that is SERPINE1, RPL26L1, PLOD2, UGDH, LGALS1, VIM, TSTA3, SORD, FDFT1, ATP2A2, MTCH2, PKP3 and JUP, within which, UGDH, TSTA3, SORD and FDFT1 were metabolic enzymes with UGDH possessing the biggest difference between the epithelial and mesenchymal cell lines. UGDH regulated SNAI1, affected cell proliferation and invasion and is associated with patient survival potentially via regulation of the intracellular GPC level. PDGFRB was involved in the regulation of UGDH in mesenchymal cells, likely through NFκB-p65. Further studies on understanding the roles of UGDH on GPC and its relationship with EMT could be valuable in developing novel therapeutics against breast cancer.

Acknowledgements

The study received funding from Icelandic centre for research award number: 163254-051; Recipient: Ottar Rolfsson and Doktorsstyrkir Háskóla Ísland; Doktorsstyrkir 2020; Recipient: Qiong Wang.

Conflict of interest

The authors declare no conflict of interest.

Author contributions

QW conceived the study, carried out the experiments, performed the data analysis, designed the figures and wrote the manuscript. STK performed the metabolomic

untargeted analysis and the flux analysis in the genome-scale metabolic network reconstructions (GEMs); FJ conducted the metabolomic experiments; AIV carried out experiments; LH, DMF and AS performed the proteomic analysis under the supervision of GS. OR conceived, supervised and funded the study, as well as analysed the data and wrote the manuscript. All authors provided critical feedbacks on the manuscript and data analysis.

Peer Review

The peer review history for this article is available at <https://publons.com/publon/10.1002/1878-0261.13172>.

Data accessibility

The mass spectrometry proteomic data have been deposited to the ProteomeXchange Consortium via the PRIDE [44] partner repository with the data set identifier [PXD024164](https://doi.org/10.1002/1878-0261.13172). The mass spectrometry phospho-proteomic data have been deposited to the ProteomeXchange Consortium via the PRIDE [44] partner repository with the data set identifier [PXD025858](https://doi.org/10.1002/1878-0261.13172).

References

- Dongre A, Weinberg RA. New insights into the mechanisms of epithelial-mesenchymal transition and implications for cancer. *Nat Rev Mol Cell Biol.* 2019;**20**:69–84. <https://doi.org/10.1038/s41580-018-0080-4>
- Brabletz T, Kalluri R, Nieto MA, Weinberg RA. EMT in cancer. *Nat Rev Cancer.* 2018;**18**:128–34. <https://doi.org/10.1038/nrc.2017.118>
- Krebs AM, Mitschke J, Lasierra Losada M, Schmalhofer O, Boerries M, Busch H, et al. The EMT-activator Zeb1 is a key factor for cell plasticity and promotes metastasis in pancreatic cancer. *Nat Cell Biol.* 2017;**19**:518–29. <https://doi.org/10.1038/ncb3513>
- Yang J, Antin P, Bex G, Blanpain C, Brabletz T, Bronner M, et al. Guidelines and definitions for research on epithelial-mesenchymal transition. *Nat Rev Mol Cell Biol.* 2020;**21**:341–52. <https://doi.org/10.1038/s41580-020-0237-9>
- Aharonov A, Shakked A, Umansky KB, Savidor A, Genzelinakh A, Kain D, et al. ERBB2 drives YAP activation and EMT-like processes during cardiac regeneration. *Nat Cell Biol.* 2020;**22**:1346–56. <https://doi.org/10.1038/s41556-020-00588-4>
- Cano A, Pérez-Moreno MA, Rodrigo I, Locascio A, Blanco MJ, del Barrio MG, et al. The transcription by repressing E-cadherin expression. *Nat Cell Biol.* 2000;**2**:76–83. <https://doi.org/10.1038/35000025>
- Tam WL, Lu H, Buikhuisen J, Soh BS, Lim E, Reinhardt F, et al. Protein kinase C alpha is a central signaling node and therapeutic target for breast cancer stem cells. *Cancer Cell.* 2013;**24**:347–64. <https://doi.org/10.1016/j.ccr.2013.08.005>
- Yu Y, Luo W, Yang ZJ, Chi JR, Li YR, Ding Y, et al. miR-190 suppresses breast cancer metastasis by regulation of TGF-beta-induced epithelial-mesenchymal transition. *Mol Cancer.* 2018;**17**:70. <https://doi.org/10.1186/s12943-018-0818-9>
- Gudjonsson T, Villadsen R, Nielsen HL, Rønnev-Jessen L, Bissell MJ, Petersen OW. Isolation, immortalization, and characterization of a human breast epithelial cell line with stem cell properties. *Genes Dev.* 2002;**16**:693–706. <https://doi.org/10.1101/gad.952602>
- Sigurdsson V, Hilmarsdottir B, Sigmundsdottir H, Fridriksdottir AJR, Ringnér M, Villadsen R, et al. Endothelial induced EMT in breast epithelial cells with stem cell properties. *PLoS One.* 2011;**6**:e23833. <https://doi.org/10.1371/journal.pone.0023833>
- Bierie B, Pierce SE, Kroeger C, Stover DG, Pattabiraman DR, Thiru P, et al. Integrin-beta4 identifies cancer stem cell-enriched populations of partially mesenchymal carcinoma cells. *Proc Natl Acad Sci USA.* 2017;**114**:E2337–46. <https://doi.org/10.1073/pnas.1618298114>
- Elenbaas B, Spirio L, Koerner F, Fleming MD, Zimonjic DB, Donaher JL, et al. Human breast cancer cells generated by oncogenic transformation of primary mammary epithelial cells. *Genes Dev.* 2001;**15**:50–65. <https://doi.org/10.1101/gad.828901>
- Ackland ML, Michalczyk A, Whitehead RH. PMC42, a novel model for the differentiated human breast. *Exp Cell Res.* 2001;**263**:14–22. <https://doi.org/10.1006/excr.2000.5106>
- Cursons J, Leuchowius KJ, Waltham M, Tomaskovic-Crook E, Foroutan M, Bracken CP, et al. Stimulus-dependent differences in signalling regulate epithelial-mesenchymal plasticity and change the effects of drugs in breast cancer cell lines. *Cell Commun Signal.* 2015;**13**:26. <https://doi.org/10.1186/s12964-015-0106-x>
- Whitehead RH, Bertoncetto I, Webber LM, Pedersen JS. A new human breast carcinoma cell line (PMC42) with stem cell characteristics. I. Morphologic characterization. *J Natl Cancer Inst.* 1983;**70**:649–61.
- Bhatia S, Monkman J, Blick T, Duijff PH, Nagaraj SH, Thompson EW. Multi-omics characterization of the spontaneous mesenchymal-epithelial transition in the PMC42 breast cancer cell lines. *J Clin Med.* 2019;**8**:1253. <https://doi.org/10.3390/jcm8081253>
- Briem E, Ingthorsson S, Traustadottir GA,

- Mol Cell Biol.* 2020;**21**:1171–72. <https://doi.org/10.1093/mcb/s41580-020-0237-9>
- 5 Aharonov A, Shakked A, Umansky KB, Savidor A, Genzelinakh A, Kain D, et al. ERBB2 drives YAP activation and EMT-like processes during cardiac regeneration. *Nat Cell Biol.* 2020;**22**:1346–56. <https://doi.org/10.1038/s41556-020-00588-4>
- 6 Cano A, Pérez-Moreno MA, Rodrigo I, Locascio A, Blanco MJ, del Barrio MG, et al. The transcription factor Snail controls epithelial–mesenchymal transitions
15. A new human breast carcinoma cell line (PMC42) with stem cell characteristics. I. Morphologic characterization. *J Natl Cancer Inst.* 1983;**70**:649–61.
- 16 Bhatia S, Monkman J, Blick T, Duijf PH, Nagaraj SH, Thompson EW. Multi-omics characterization of the spontaneous mesenchymal-epithelial transition in the PMC42 breast cancer cell lines. *J Clin Med.* 2019;**8**:1253. <https://doi.org/10.3390/jcm8081253>
- 17 Briem E, Ingthorsson S, Traustadottir GA, Hilmarsdottir B, Gudjonsson T. Application of the

- D492 cell lines to explore breast morphogenesis, EMT and cancer progression in 3D culture. *J Mammary Gland Biol Neoplasia*. 2019;**24**:139–47. <https://doi.org/10.1007/s10911-018-09424-w>
- 18 Kröger C, Afeyan A, Mraz J, Eaton EN, Reinhardt F, Khodor YL, et al. Acquisition of a hybrid E/M state is essential for tumorigenicity of basal breast cancer cells. *Proc Natl Acad Sci USA*. 2019;**116**:7353–62. <https://doi.org/10.1073/pnas.1812876116>
 - 19 Morandi A, Taddei ML, Chiarugi P, Giannoni E. Targeting the metabolic reprogramming that controls epithelial-to-mesenchymal transition in aggressive tumors. *Front Oncol*. 2017;**7**:40. <https://doi.org/10.3389/fonc.2017.00040>
 - 20 Li M, Bu X, Cai B, Liang P, Li K, Qu X, et al. Biological role of metabolic reprogramming of cancer cells during epithelial mesenchymal transition (Review). *Oncol Rep*. 2019;**41**:727–41. <https://doi.org/10.3892/or.2018.6882>
 - 21 Williams ED, Gao D, Redfern A, Thompson EW. Controversies around epithelial-mesenchymal plasticity in cancer metastasis. *Nat Rev Cancer*. 2019;**19**:716–32. <https://doi.org/10.1038/s41568-019-0213-x>
 - 22 Eiriksson FF, Rolfsson O, Ogmundsdottir HM, Haraldsson GG, Thorsteinsdottir M, Halldorsson S. Altered plasmalogen content and fatty acid saturation following epithelial to mesenchymal transition in breast epithelial cell lines. *Int J Biochem Cell Biol*. 2018;**103**:99–104. <https://doi.org/10.1016/j.biocel.2018.08.003>
 - 23 Halldorsson S, Rohatgi N, Magnusdottir M, Choudhary KS, Gudjonsson T, Knutsen E, et al. Metabolic re-wiring of isogenic breast epithelial cell lines following epithelial to mesenchymal transition. *Cancer Lett*. 2017;**396**:117–29. <https://doi.org/10.1016/j.canlet.2017.03.019>
 - 24 Karvelsson ST, Sigurdsson A, Seip K, Grinde MT, Wang Q, Johannsson F, et al. EMT-derived alterations in glutamine metabolism sensitize mesenchymal breast cells to mTOR inhibition. *Mol Cancer Res*. 2021;**19**:1546–58. <https://doi.org/10.1158/1541-7786.MCR-20-0962>
 - 25 Karvelsson ST, Wang Q, Hilmarsdottir B, Sigurdsson A, Moestue SA, Maclandsmo GM, et al. Argininosuccinate lyase is a metabolic vulnerability in breast development and cancer. *NPJ Syst Biol Appl*. 2021;**7**:36. <https://doi.org/10.1038/s41540-021-00195-5>
 - 26 Wang Q, Karvelsson ST, Kotronoulas A, Gudjonsson T, Halldorsson S, Rolfsson O. Glutamine-fructose-6-phosphate transaminase 2 (GFPT2) is upregulated in breast epithelial-mesenchymal transition and responds to oxidative stress. *Mol Cell Proteomics*. 2021, in press. <https://doi.org/10.1016/j.mcpro.2021.100185>
 - 27 Arnold JM, Gu F, Ambati CR, Rasaily U, Ramirez-Pena E, Joseph R, et al. UDP-glucose 6-dehydrogenase regulates hyaluronic acid production and promotes breast cancer progression. *Oncogene*. 2020;**39**:3089–101. <https://doi.org/10.1038/s41388-019-0885-4>
 - 28 Wang X, Liu R, Zhu W, Chu H, Yu H, Wei P, et al. UDP-glucose accelerates SNAIL mRNA decay and impairs lung cancer metastasis. *Nature*. 2019;**571**:127–31. <https://doi.org/10.1038/s41586-019-1340-y>
 - 29 Bontemps Y, Vuillermoz B, Antonicelli F, Perreau C, Danan JL, Maquart FX, et al. Specific protein-1 is a universal regulator of UDP-glucose dehydrogenase expression: its positive involvement in transforming growth factor-beta signaling and inhibition in hypoxia. *J Biol Chem*. 2003;**278**:21566–75. <https://doi.org/10.1074/jbc.M209366200>
 - 30 Clarkin CE, Allen S, Kuiper NJ, Wheeler BT, Wheeler-Jones CP, Pitsillides AA. Regulation of UDP-glucose dehydrogenase is sufficient to modulate hyaluronan production and release, control sulfated GAG synthesis, and promote chondrogenesis. *J Cell Physiol*. 2011;**226**:749–61. <https://doi.org/10.1002/jcp.22393>
 - 31 Fernando R, Smith TJ. Slit2 regulates hyaluronan & cytokine synthesis in fibrocytes: potential relevance to thyroid associated ophthalmopathy. *J Clin Endocrinol Metab*. 2021;**106**:e20–33. <https://doi.org/10.1210/clinem/dgaa684>
 - 32 Lin LH, Chou HC, Chang SJ, Liao EC, Tsai YT, Wei YS, et al. Targeting UDP-glucose dehydrogenase inhibits ovarian cancer growth and metastasis. *J Cell Mol Med*. 2020;**24**:11883–902. <https://doi.org/10.1111/jcmm.15808>
 - 33 Pan YR, Vatsyayan J, Chang YS, Chang HY. Epstein-Barr virus latent membrane protein 2A upregulates UDP-glucose dehydrogenase gene expression via ERK and PI3K/Akt pathway. *Cell Microbiol*. 2008;**10**:2447–60. <https://doi.org/10.1111/j.1462-5822.2008.01221.x>
 - 34 Teoh ST, Ogrodzinski MP, Lunt SY. UDP-glucose 6-dehydrogenase knockout impairs migration and decreases in vivo metastatic ability of breast cancer cells. *Cancer Lett*. 2020;**492**:21–30. <https://doi.org/10.1016/j.canlet.2020.07.031>
 - 35 Goodwin CR, Ahmed AK, Xia S. UDP- α -D-glucose 6-dehydrogenase: a promising target for glioblastoma. *Oncotarget*. 2019;**10**:1542–3. <https://doi.org/10.18632/oncotarget.26670>
 - 36 Huang D, Casale GP, Tian J, Lele SM, Pisarev VM, Simpson MA, et al. Udp-glucose dehydrogenase as a novel field-specific candidate biomarker of prostate cancer. *Int J Cancer*. 2010;**126**:315–27. <https://doi.org/10.1002/ijc.24820>
 - 37 Oyinlade O, Wei S, Lal B, Larterra J, Zhu H, Goodwin CR, et al. Targeting UDP-alpha-D-glucose 6-dehydrogenase inhibits glioblastoma growth and migration. *Oncogene*. 2018;**37**:2615–29. <https://doi.org/10.1038/s41388-018-0138-y>

- 38 Ingthorsson S, Andersen K, Hilmarsdottir B, Maelandsmo GM, Magnusson MK, Gudjonsson T. HER2 induced EMT and tumorigenicity in breast epithelial progenitor cells is inhibited by coexpression of EGFR. *Oncogene*. 2016;**35**:4244–55. <https://doi.org/10.1038/onc.2015.489>
- 39 Rappsilber J, Ishihama Y, Mann M. Stop and go extraction tips for matrix-assisted laser desorption/ionization, nanoelectrospray, and LC/MS sample pretreatment in proteomics. *Anal Chem*. 2003;**75**:663–70. <https://doi.org/10.1021/ac026117i>
- 40 Aass KR, Mjelle R, Kastnes MH, Tryggestad SS, van den Brink LM, Westhryn M, et al. IL-32 is a metabolic regulator promoting survival and proliferation of malignant plasma cells. *bioRxiv*. 2021. <https://doi.org/10.1101/2021.02.22.431638>
- 41 Kil YJ, Becker C, Sandoval W, Goldberg D, Bern M. Preview: a program for surveying shotgun proteomics tandem mass spectrometry data. *Anal Chem*. 2011;**83**:5259–67. <https://doi.org/10.1021/ac200609a>
- 42 Eng JK, McCormack AL, Yates JR. An approach to correlate tandem mass spectral data of peptides with amino acid sequences in a protein database. *J Am Soc Mass Spectrom*. 1994;**5**:976–89. [https://doi.org/10.1016/1044-0305\(94\)80016-2](https://doi.org/10.1016/1044-0305(94)80016-2)
- 43 Horn M, Ueckert T, Fritzsche K, Tham K, Paschke C, Berg F, Pfaff H, Jiang X, Li S, Lopez-Ferrer D. New method for label-free quantification in the Proteome Discoverer framework. 2016.
- 44 Perez-Riverol Y, Csordas A, Bai J, Bernal-Llinares M, Hewapathirana S, Kundu DJ, et al. The PRIDE database and related tools and resources in 2019: improving support for quantification data. *Nucleic Acids Res*. 2018;**47**:D442–50. <https://doi.org/10.1093/nar/gky1106>
- 45 Cox J, Mann M. MaxQuant enables high peptide identification rates, individualized p.p.b.-range mass accuracies and proteome-wide protein quantification. *Nat Biotechnol*. 2008;**26**:1367–72. <https://doi.org/10.1038/nbt.1511>
- 46 Cox J, Neuhauser N, Michalski A, Scheltema RA, Olsen JV, Mann M. Andromeda: a peptide search engine integrated into the MaxQuant environment. *J Proteome Res*. 2011;**10**:1794–805. <https://doi.org/10.1021/pr101065j>
- 47 Rolfsson O, Johannsson F, Magnúsdóttir M, Paglia G, Sigurjonsson OE, Bordbar A, et al. Mannose and fructose metabolism in red blood cells during cold storage in SAGM. *Transfusion*. 2017;**57**:2665–76. <https://doi.org/10.1111/trf.14266>
- 48 Smith CA, Want EJ, O'Maille G, Abagyan R, Siuzdak G. XCMS: processing mass spectrometry data for metabolite profiling using nonlinear peak alignment, matching, and identification. *Anal Chem*. 2006;**78**:779–
- 49 Tautenhahn R, Böttcher C, Neumann S. Highly sensitive feature detection for high resolution LC/MS. *BMC Bioinformatics*. 2008;**9**:504. <https://doi.org/10.1186/1471-2105-9-504>
- 50 Tsugawa H, Cajka T, Kind T, Ma Y, Higgins B, Ikeda K, et al. MS-DIAL: data-independent MS/MS deconvolution for comprehensive metabolome analysis. *Nat Methods*. 2015;**12**:523–6. <https://doi.org/10.1038/nmeth.3393>
- 51 Dunn WB, Broadhurst D, Begley P, Zelena E, Francis-McIntyre S, Anderson N, et al. Procedures for large-scale metabolic profiling of serum and plasma using gas chromatography and liquid chromatography coupled to mass spectrometry. *Nat Protoc*. 2011;**6**:1060–83. <https://doi.org/10.1038/nprot.2011.335>
- 52 De Livera AM, Olshansky G, Simpson JA, Creek DJ. NormalizeMets: assessing, selecting and implementing statistical methods for normalizing metabolomics data. *Metabolomics*. 2018;**14**:54. <https://doi.org/10.1007/s11306-018-1347-7>
- 53 Durbin BP, Hardin JS, Hawkins DM, Rocke DM. A variance-stabilizing transformation for gene-expression microarray data. *Bioinformatics*. 2002;**18**:S105–10. https://doi.org/10.1093/bioinformatics/18.suppl_1.S105
- 54 Tyanova S, Temu T, Sinitcyn P, Carlson A, Hein MY, Geiger T, et al. The Perseus computational platform for comprehensive analysis of (prote)omics data. *Nat Methods*. 2016;**13**:731–40. <https://doi.org/10.1038/nmeth.3901>
- 55 Huang DW, Sherman BT, Lempicki RA. Bioinformatics enrichment tools: paths toward the comprehensive functional analysis of large gene lists. *Nucleic Acids Res*. 2009;**37**:1–13. <https://doi.org/10.1093/nar/gkn923>
- 56 Huang DW, Sherman BT, Lempicki RA. Systematic and integrative analysis of large gene lists using DAVID bioinformatics resources. *Nat Protoc*. 2009;**4**:44–57. <https://doi.org/10.1038/nprot.2008.211>
- 57 Jassal B, Matthews L, Viteri G, Gong C, Lorente P, Fabregat A, et al. The reactome pathway knowledgebase. *Nucleic Acids Res*. 2019;**48**:D498–503. <https://doi.org/10.1093/nar/gkz1031>
- 58 Györfi B, Lanczky A, Eklund AC, Denkert C, Budczies J, Li Q, et al. An online survival analysis tool to rapidly assess the effect of 22,277 genes on breast cancer prognosis using microarray data of 1,809 patients. *Breast Cancer Res Treat*. 2010;**123**:725–31. <https://doi.org/10.1007/s10549-009-0674-9>
- 59 Zhao M, Liu Y, Zheng C, Qu H. dbEMT 2.0: an updated database for epithelial-mesenchymal transition genes with experimentally verified information and precalculated regulation information for cancer metastasis. *J Genet Genomics*. 2019;**46**:595–7. <https://doi.org/10.1007/s11427-019-0674-9>

- 47 Renesson O, Johannsson F, Magnúsdóttir M, Pagna G, Sigurjonsson OE, Bordbar A, et al. Mannose and fructose metabolism in red blood cells during cold storage in SAGM. *Transfusion*. 2017;**57**:2665–76. <https://doi.org/10.1111/trf.14266>
- 48 Smith CA, Want EJ, O'Maille G, Abagyan R, Siuzdak G. XCMS: processing mass spectrometry data for metabolite profiling using nonlinear peak alignment, matching, and identification. *Anal Chem*. 2006;**78**:779–87. <https://doi.org/10.1021/ac051437y>
- 49 Zhang Y, Wang Y, Wang Y, Wang Y, Wang Y, Wang Y, et al. To rapidly assess the effect of 22,277 genes on breast cancer prognosis using microarray data of 1,809 patients. *Breast Cancer Res Treat*. 2010;**123**:725–31. <https://doi.org/10.1007/s10549-009-0674-9>
- 50 Zhao M, Liu Y, Zheng C, Qu H. dbEMT 2.0: an updated database for epithelial-mesenchymal transition genes with experimentally verified information and precalculated regulation information for cancer metastasis. *J Genet Genomics*. 2019;**46**:595–7. <https://doi.org/10.1016/j.jgg.2019.11.010>

- 60 Loh CY, Chai JY, Tang TF, Wong WF, Sethi G, Shanmugam MK, et al. The E-cadherin and N-cadherin switch in epithelial-to-mesenchymal transition: signaling, therapeutic implications, and challenges. *Cells*. 2019;**8**:1118. <https://doi.org/10.3390/cells8101118>
- 61 Freeze HH, Hart GW, Schnaar RL. Glycosylation precursors. In: Varki A, Cummings RD, Esko JD, Stanley P, Hart GW, Aebi M, et al. editors. *Essentials of glycobiology*. Cold Spring Harbor, NY: Cold Spring Harbor Laboratory Press; 2015. p. 51–63.
- 62 Li H, Ning S, Ghandi M, Kryukov GV, Gopal S, Deik A, et al. The landscape of cancer cell line metabolism. *Nat Med*. 2019;**25**:850–60. <https://doi.org/10.1038/s41591-019-0404-8>
- 63 Shaul YD, Freinkman E, Comb WC, Cantor JR, Tam WL, Thiru P, et al. Dihydropyrimidine accumulation is required for the epithelial-mesenchymal transition. *Cell*. 2014;**158**:1094–109. <https://doi.org/10.1016/j.cell.2014.07.032>
- 64 Steinhäuser SS, Morera E, Budkova Z, Schepsky A, Wang Q, Rolfsson O, et al. ECM1 secreted by HER2-overexpressing breast cancer cells promotes formation of a vascular niche accelerating cancer cell migration and invasion. *Lab Invest*. 2020;**100**:928–44. <https://doi.org/10.1038/s41374-020-0415-6>
- 65 Barkovskaya A, Goodwin CM, Seip K, Hilmarsdottir B, Pettersen S, Stalneck C, et al. Detection of phenotype-specific therapeutic vulnerabilities in breast cells using a CRISPR loss-of-function screen. *Mol Oncol*. 2021;**15**:2026–45. <https://doi.org/10.1002/1878-0261.12951>
- 66 Aigner K, Descovich L, Mikula M, Sultan A, Dampier B, Bonné S, et al. The transcription factor ZEB1 (deltaEF1) represses Plakophilin 3 during human cancer progression. *FEBS Lett*. 2007;**581**:1617–24. <https://doi.org/10.1016/j.febslet.2007.03.026>
- 67 Bacigalupo ML, Manzi M, Espelt MV, Gentilini LD, Compagno D, Laderach DJ, et al. Galectin-1 triggers epithelial-mesenchymal transition in human hepatocellular carcinoma cells. *J Cell Physiol*. 2015;**230**:1298–309. <https://doi.org/10.1002/jcp.24865>
- 68 Bedi U, Mishra VK, Wasilewski D, Scheel C, Johnsen SA. Epigenetic plasticity: a central regulator of epithelial-to-mesenchymal transition in cancer. *Oncotarget*. 2014;**5**:2016–29. <https://doi.org/10.18632/oncotarget.1875>
- 69 Li H, Zhong A, Li S, Meng X, Wang X, Xu F, et al. The integrated pathway of TGFβ/Snail with TNFα/NFκB may facilitate the tumor-stroma interaction in the EMT process and colorectal cancer prognosis. *Sci Rep*. 2017;**7**:4915. <https://doi.org/10.1038/s41598-017-05280-6>
- 70 Pavón M, Parreño M, Téllez-Gabriel M, Sancho F, López M, Céspedes M, et al. Gene expression signatures and molecular markers associated with clinical outcome in locally advanced head and neck carcinoma. *Carcinogenesis*. 2012;**33**:1707–16. <https://doi.org/10.1093/carcin/bgs207>
- 71 Xu F, Zhang J, Hu G, Liu L, Liang W. Hypoxia and TGF-β1 induced PLOD2 expression improve the migration and invasion of cervical cancer cells by promoting epithelial-to-mesenchymal transition (EMT) and focal adhesion formation. *Cancer Cell Int*. 2017;**17**:54. <https://doi.org/10.1186/s12935-017-0420-z>
- 72 Yamagami Y, Kawami M, Ojima T, Futatsugi S, Yumoto R, Takano M. Role of plasminogen activator inhibitor-1 in methotrexate-induced epithelial-mesenchymal transition in alveolar epithelial A549 cells. *Biochem Biophys Res Comm*. 2020;**525**:543–8. <https://doi.org/10.1016/j.bbrc.2020.02.131>
- 73 Mendez MG, Kojima S-I, Goldman RD. Vimentin induces changes in cell shape, motility, and adhesion during the epithelial to mesenchymal transition. *FASEB J*. 2010;**24**:1838–51. <https://doi.org/10.1096/fj.09-151639>
- 74 Hugo H, Ackland ML, Blick T, Lawrence MG, Clements JA, Williams ED, et al. Epithelial-mesenchymal and mesenchymal-epithelial transitions in carcinoma progression. *J Cell Physiol*. 2007;**213**:374–83. <https://doi.org/10.1002/jcp.21223>
- 75 Vergara D, Simeone P, Latorre D, Cascione F, Leporatti S, Trerotola M, et al. Proteomics analysis of E-cadherin knockdown in epithelial breast cancer cells. *J Biotechnol*. 2015;**202**:3–11. <https://doi.org/10.1016/j.jbiotec.2014.10.034>
- 76 Vitale DL, Caon I, Parnigoni A, Sevic I, Spinelli FM, Icardi A, et al. Initial identification of UDP-glucose dehydrogenase as a prognostic marker in breast cancer patients, which facilitates epirubicin resistance and regulates hyaluronan synthesis in MDA-MB-231 cells. *Biomolecules*. 2021;**11**:246.
- 77 Sonkar K, Ayyappan V, Tressler CM, Adelaja O, Cai R, Cheng M, et al. Focus on the glycerophosphocholine pathway in choline phospholipid metabolism of cancer. *NMR Biomed*. 2019;**32**:e4112. <https://doi.org/10.1002/nbm.4112>
- 78 Cao MD, Sitter B, Bathen TF, Bofin A, Lønning PE, Lundgren S, et al. Predicting long-term survival and treatment response in breast cancer patients receiving neoadjuvant chemotherapy by MR metabolic profiling. *NMR Biomed*. 2012;**25**:369–78. <https://doi.org/10.1002/nbm.1762>
- 79 Giskeødegård GF, Grinde MT, Sitter B, Axelson DE, Lundgren S, Fjøsne HE, et al. Multivariate modeling and prediction of breast cancer prognostic factors using MR metabolomics. *J Proteome Res*. 2010;**9**:972–9. <https://doi.org/10.1021/pr9008783>
- 80 Moestue SA, Borgan E, Huuse EM, Lindholm EM, Sitter B, Børresen-Dale A-L, et al. Distinct choline

- metabolic profiles are associated with differences in gene expression for basal-like and luminal-like breast cancer xenograft models. *BMC Cancer*. 2010;**10**:433. <https://doi.org/10.1186/1471-2407-10-433>
- 81 Pommier RM, Sanlaville A, Tonon L, Kielbassa J, Thomas E, Ferrari A, et al. Comprehensive characterization of claudin-low breast tumors reflects the impact of the cell-of-origin on cancer evolution. *Nat Commun*. 2020;**11**:3431. <https://doi.org/10.1038/s41467-020-17249-7>
 - 82 Fougner C, Bergholtz H, Norum JH, Sorlie T. Re-definition of claudin-low as a breast cancer phenotype. *Nat Commun*. 2020;**11**:1787. <https://doi.org/10.1038/s41467-020-15574-5>
 - 83 Bharti SK, Mironchik Y, Wildes F, Penet MF, Goggins E, Krishnamachary B, et al. Metabolic consequences of HIF silencing in a triple negative human breast cancer xenograft. *Oncotarget*. 2018;**9**:15326–39. <https://doi.org/10.18632/oncotarget.24569>
 - 84 Koch K, Hartmann R, Schröter F, Suwala AK, Maciaczyk D, Krüger AC, et al. Reciprocal regulation of the cholinic phenotype and epithelial-mesenchymal transition in glioblastoma cells. *Oncotarget*. 2016;**7**:73414–31. <https://doi.org/10.18632/oncotarget.12337>
 - 85 Okazaki Y, Nakamura K, Takeda S, Yoshizawa I, Yoshida F, Ohshima N, et al. GDE5 inhibition accumulates intracellular glycerophosphocholine and suppresses adipogenesis at a mitotic clonal expansion stage. *Am J Physiol Cell Physiol*. 2019;**316**:C162–74. <https://doi.org/10.1152/ajpcell.00305.2018>
 - 86 Ahmadian M, Suh JM, Hah N, Liddle C, Atkins AR, Downes M, et al. PPARgamma signaling and metabolism: the good, the bad and the future. *Nat Med*. 2013;**19**:557–66. <https://doi.org/10.1038/nm.3159>
 - 87 Tontonoz P, Spiegelman BM. Fat and beyond: the diverse biology of PPARgamma. *Annu Rev Biochem*. 2008;**77**:289–312. <https://doi.org/10.1146/annurev.biochem.77.061307.091829>
 - 88 Iorio E, Mezzanzanica D, Alberti P, Spadaro F, Ramoni C, D'Ascenzo S, et al. Alterations of choline phospholipid metabolism in ovarian tumor progression. *Cancer Res*. 2005;**65**:9369–76. <https://doi.org/10.1158/0008-5472.CAN-05-1146>
 - 89 Menzel N, Fischl W, Hueging K, Bankwitz D, Frentzen A, Haid S, et al. MAP-kinase regulated cytosolic phospholipase A2 activity is essential for production of infectious hepatitis C virus particles. *PLoS Pathog*. 2012;**8**:e1002829. <https://doi.org/10.1371/journal.ppat.1002829>
 - 90 Ulisse S, Cinque B, Silvano G, Rucci N, Biordi L, Cifone MG, et al. Erk-dependent cytosolic phospholipase A2 activity is induced by CD95 ligand and is required to trigger apoptosis in CD95 bearing cells. *Cell Death Differ*. 2000;**7**:916–24. <https://doi.org/10.1038/sj.cdd.4400716>
 - 91 Huber MA, Azoitei N, Baumann B, Grunert S, Sommer A, Pehamberger H, et al. NF-kappaB is essential for epithelial-mesenchymal transition and metastasis in a model of breast cancer progression. *J Clin Invest*. 2004;**114**:569–81. <https://doi.org/10.1172/JCI21358>
 - 92 Naidu S, Shi L, Magee P, Middleton JD, Laganá A, Sahoo S, et al. PDGFR-modulated miR-23b cluster and miR-125a-5p suppress lung tumorigenesis by targeting multiple components of KRAS and NF-kB pathways. *Sci Rep*. 2017;**7**:15441. <https://doi.org/10.1038/s41598-017-14843-6>
 - 93 Wang H, Yin Y, Li W, Zhao X, Yu Y, Zhu J, et al. Over-expression of PDGFR-beta promotes PDGF-induced proliferation, migration, and angiogenesis of EPCs through PI3K/Akt signaling pathway. *PLoS One*. 2012;**7**:e30503. <https://doi.org/10.1371/journal.pone.0030503>
 - 94 Wang Z, Ahmad A, Li Y, Kong D, Azmi AS, Banerjee S, et al. Emerging roles of PDGF-D signaling pathway in tumor development and progression. *Biochem Biophys Acta*. 2010;**1806**:122–30. <https://doi.org/10.1016/j.bbcan.2010.04.003>
 - 95 Wu Q, Wang R, Yang Q, Hou X, Chen S, Hou Y, et al. Chemoresistance to gemcitabine in hepatoma cells induces epithelial-mesenchymal transition and involves activation of PDGF-D pathway. *Oncotarget*. 2013;**4**:1999–2009.
 - 96 Shimamura T, Hsu TC, Colburn NH, Bejcek BE. Activation of NF-kappaB is required for PDGF-B chain to transform NIH3T3 cells. *Exp Cell Res*. 2002;**274**:157–67. <https://doi.org/10.1006/excr.2001.5449>
 - 97 Xu B, Bai Z, Yin J, Zhang Z. Global transcriptomic analysis identifies SERPINE1 as a prognostic biomarker associated with epithelial-to-mesenchymal transition in gastric cancer. *PeerJ*. 2019;**7**:e7091. <https://doi.org/10.7717/peerj.7091>
 - 98 Piskareva O, Harvey H, Nolan J, Conlon R, Alcock L, Buckley P, et al. The development of cisplatin resistance in neuroblastoma is accompanied by epithelial to mesenchymal transition in vitro. *Cancer Lett*. 2015;**364**:142–55. <https://doi.org/10.1016/j.canlet.2015.05.004>
 - 99 Ren B-J, Zhou Z-W, Zhu D-J, Ju Y-L, Wu J-H, Ouyang M-Z, et al. Alisertib induces cell cycle arrest, apoptosis, autophagy and suppresses EMT in HT29 and Caco-2 cells. *Int J Mol Sci*. 2015;**17**:41. <https://doi.org/10.3390/ijms17010041>
 - 100 Wang Y, Zeng G, Jiang Y. The emerging roles of miR-125b in cancers. *Cancer Manag Res*.

- 89 Menzel A, Felsen W, Raegling A, Bankwitz L, Frentzen A, Haid S, et al. MAP-kinase regulated cytosolic phospholipase A2 activity is essential for production of infectious hepatitis C virus particles. *PLoS Pathog.* 2012;**8**:e1002829. <https://doi.org/10.1371/journal.ppat.1002829>
- 90 Ulisse S, Cinque B, Silvano G, Rucci N, Biordi L, Cifone MG, et al. Erk-dependent cytosolic phospholipase A2 activity is induced by CD95 ligand cross-linking in the mouse derived sertoli cell line TM4 *Cell.* 2019;**177**:112–25. <https://doi.org/10.1016/j.cell.2015.05.004>
- 99 Ren B-J, Zhou Z-W, Zhu D-J, Ju Y-L, Wu J-H, Ouyang M-Z, et al. Alisertib induces cell cycle arrest, apoptosis, autophagy and suppresses EMT in HT29 and Caco-2 cells. *Int J Mol Sci.* 2015;**17**:41. <https://doi.org/10.3390/ijms17010041>
- 100 Wang Y, Zeng G, Jiang Y. The emerging roles of miR-125b in cancers. *Cancer Manag Res.* 2020;**12**:1079–88. <https://doi.org/10.2147/cmar.S232388>

- 101 Schwab A, Siddiqui A, Vazakidou ME, Napoli F, Böttcher M, Menchicchi B, et al. Polyol pathway links glucose metabolism to the aggressiveness of cancer cells. *Cancer Res.* 2018;**78**:1604–18. <https://doi.org/10.1158/0008-5472.Can-17-2834>
- 102 Yang Y-F, Chang Y-C, Jan Y-H, Yang C-J, Huang M-S, Hsiao M. Squalene synthase promotes the invasion of lung cancer cells via the osteopontin/ERK pathway. *Oncogenesis.* 2020;**9**:78. <https://doi.org/10.1038/s41389-020-00262-2>
- 103 Davis FM, Parsonage MT, Cabot PJ, Parat M-O, Thompson EW, Roberts-Thomson SJ, et al. Assessment of gene expression of intracellular calcium channels, pumps and exchangers with epidermal growth factor-induced epithelial-mesenchymal transition in a breast cancer cell line. *Cancer Cell Int.* 2013;**13**:76. <https://doi.org/10.1186/1475-2867-13-76>
- 104 Demirkan B. The roles of epithelial-to-mesenchymal transition (EMT) and mesenchymal-to-epithelial transition (MET) in breast cancer bone metastasis: potential targets for prevention and treatment. *J Clin Med.* 2013;**2**:264–82. <https://doi.org/10.3390/jcm2040264>
- 105 Lourenco AR, Ban Y, Crowley MJ, Lee SB, Ramchandani D, Du W, et al. Differential contributions of pre- and post-EMT tumor cells in breast cancer metastasis. *Can Res.* 2020;**80**:163–9. <https://doi.org/10.1158/0008-5472.Can-19-1427>

Supporting information

Additional supporting information may be found online in the Supporting Information section at the end of the article.

Fig. S1. Study workflow and the phenotypes of the cell lines. (A) Workflow of the proteomic analysis of the three breast EMT cell models and metabolomics analysis after siRNA knock-down of the metabolic target *UGDH* in all the mesenchymal cell lines. Three breast EMT cell models (epithelial and mesenchymal cell line pairs) were used in this study, D492&D492M, HMLE&HMLEM, and PMC42LA&PMC42ET. The proteomic strategy was label-free quantification (LFQ) with each cell line in triplicates. The metabolomic strategy was untargeted metabolomics in negative, positive, and basic modes with six replicates. The upstream signaling regulation and downstream cellular functions of *UGDH* were also investigated in this study. The tumorigenic breast mesenchymal cell line D492HER2 and malignant MDA-MB-231 were employed further to define the functions of *UGDH* in tumor malignancy. (B) Photos of all the cell lines in the three breast EMT cell models used in this study were shown. Different cell lines were cultured in their

routine maintaining medium respectively, and the photos were taken under phase contrast with objectives 5x or 20x.

Fig. S2. Inconsistent EMT markers. A list of known EMT markers (based on the public EMT database dbEMT) was inconsistently altered among the three EMT models. Student's T-test, *: $P < 0.05$; **: $P < 0.01$; ***: $P < 0.001$; $n = 3$. CD44, CD44 antigen; LMNB1, Lamin-B1; MSN, Moesin; FLNA, Filamin-A; TLN1, Talin-1; FSCN1, Fascin; EGFR, Epidermal growth factor receptor; S100A2, S100 calcium binding protein A2; NDRG1, N-myc downstream regulated 1.

Fig. S3. Accuracy and validity of the proteomic analysis. The accuracy and validity of the proteomic analysis in this study were confirmed by comparing the current data to our previously generated proteomic data for the D492 EMT model [26]. The correlation between these two datasets was 0.936. The high correlation coefficient (Pearson correlation, 0.936) of the datasets ensures good accuracy and validity of the proteomic analysis in this study. It laid the foundation for valid conclusions deduced from this study.

Fig. S4. Functional annotation of the GO terms (CC and MF) for the three EMT models. Functional annotation of the GO terms (CC and MF) was conducted on the DAVID (DAVID Bioinformatics Resources 6.8) platform for each EMT model. Data used for the GO annotation analysis (Supplementary Table 3) were proteins significantly altered in each EMT model (Permutation-based FDR < 0.05). Default settings were used for the analysis. The GO terms were listed according to the $-\log_{10}$ p value in descending order. The numbers of genes in each GO term were also plotted as dots/line plots. CC: Cellular Component; MF: Molecular Function.

Fig. S5. Knock-down efficiency of *UGDH* with two siRNAs. (A-D) The knock-down efficiency of *UGDH* with two siRNAs compared to the scramble control was around 80 % in D492M ($n = 7$ for the first siRNA; $n = 9$ for the second siRNA) (A-B) and 60 % in D492HER2 ($n = 5$) (C-D). (E) The knock-down efficiency of *UGDH* with two siRNAs in the metabolomics experiments for D492M, HMELM, and PMC42ET was 90 % ($n = 5$). KD: Knock-down. Student's T-test, ***: $P < 0.001$. *UGDH*, UDP-glucose 6-dehydrogenase.

Fig. S6. Functional analysis of *UGDH* in EMT. (A) Photos of the D492M and D492HER2 cells following knock-down of *UGDH* via two siRNAs in the invasion assay. Cells were stained with DAPI and observed under the objective 10x. (B-C) Cell invasion decreased with the second siRNA knock-down of *UGDH* in both non-tumorigenic D492M (B) and tumorigenic

D492HER2 (C). *n* equals 3, and ten spots were chosen for each replicate during the cell counting process. (D-E) One of the main EMT transcription factors *SNAIL* was downregulated following the second siRNA knock-down of *UGDH* in both non-tumorigenic D492M (*n* = 5) (D) and tumorigenic D492HER2 (*n* = 4) (E). (F-H) The Kaplan-Meier plots of *FDFT1*, *SORD*, and *TSTA3* in basal breast cancer patients were downloaded from kmplot.com. Student's T-test, **: *P* < 0.01; ***: *P* < 0.001. *UGDH*, UDP-glucose 6-dehydrogenase; *SNAIL*, Snail Family Transcriptional Repressor 1; *FDFT1*, Squalene synthase; *SORD*, Sorbitol dehydrogenase; *TSTA3*, GDP-L-fucose synthase.

Fig. S7. GPC and NAA were altered with the siUGDH treatment in D492HER2 and MDA-MB-231. (A-D) The glycerophosphocholine (GPC) level was decreased, and the acetylaspartate (NAA) level was increased after the siUGDH treatment in the tumorigenic D492HER2 (*n* = 3) and malignant MDA-MB-231 (*n* = 6) cell lines. (E) There were no significant differences to the GPC levels between mesenchymal cells and non-mesenchymal cells based on published datasets in literature [62, 63] (Supplementary Table 5). (F-G) The expression levels of choline (F) and phosphocholine (G) with *UGDH* knock-down in the three EMT cell models. No significant and consistent changes were observed for both metabolites in all the cell lines (*n* = 5). (H) *UGDH* has been reported to downregulate *PPAR* γ [27]. To test if there was a negative correlation between *UGDH* and *PPAR* signaling, we performed a phosphoproteomic analysis on the D492 EMT cell model (Supplementary Table 7) and noticed that the *PPAR* signaling was downregulated in the mesenchymal cells where *UGDH* was highly expressed. The IPA pathways were listed based on the $-\log_{10}(p \text{ value})$, and the z-scores for the pathways were represented by the dots/line plot. Red: higher in the mesenchymal D492M; blue: higher in the epithelial D492. (I) The enzyme *PLA2G15* potentially involved in the hydrolysis of phosphatidylcholine (PtdCho) into GPC was higher in both D492M and D492HER2. *UGDH* has been reported to regulate the phosphorylation of *ERK* (pERK) [32]. cPLA2 is responsible for GPC synthesis from PtdCho in choline metabolism

and is under the control of *ERK*/*MAPK* [89, 90]. We also observed that *PLA2G15* was highly expressed in D492M and D492HER2 compared to D492 (I), suggesting the knock-down of *UGDH* may downregulate GPC via pERK-*PLA2G15* (*n* = 3). Student's T-test, *: *P* < 0.05; **: *P* < 0.01; ***: *P* < 0.001. n.s: not significant. *UGDH*, UDP-glucose 6-dehydrogenase; *PLA2G15*, Phospholipase A2 group XV. **Fig. S8.** *PDGFRB* regulates *UGDH* via *RELA* (NF κ B-p65). (A) *PDGFRB* was highly expressed in the tumorigenic mesenchymal cell line D492HER2 based on the RPPA analysis (*n* = 3) [65]. (B) The knock-down efficiency of *PDGFRB* with siRNA in the D492HER2 cell line was about 90 % (*n* = 6). (C) *RELA* (NF κ B-p65) was downregulated after the siRNA knock-down of *PDGFRB* in D492HER2 (*n* = 6). (D) *UGDH* was downregulated after the siRNA knock-down of *PDGFRB* in D492HER2 (*n* = 6). (E) The knock-down efficiency of *RELA* with the second siRNA in D492M was around 70 % (*n* = 6). (F) *UGDH* was downregulated after the knock-down of *RELA* in D492M with the second siRNA (*n* = 6). (G) The knock-down efficiency of *RELA* with the first siRNA in D492HER2 was around 90 % (*n* = 6). (H) No significant change in *UGDH* was observed after the knock-down of *RELA* with the first siRNA in D492HER2 (*n* = 6). (I) The knock-down efficiency of *RELA* with the second siRNA in the D492HER2 cell line was about 90 % (*n* = 6). (J) *UGDH* was downregulated after the knock-down of *RELA* in D492HER2 with the second siRNA (*n* = 6). Student's T-test, *: *P* < 0.05; **: *P* < 0.01; ***: *P* < 0.001. *UGDH*, UDP-glucose 6-dehydrogenase; *PDGFRB*, Platelet-derived growth factor receptor beta; *RELA* (NF κ B-p65), Nuclear factor NF-kappa-B p65 subunit.

Table S1. The internal standard mix used in the metabolomics analysis.

Table S2. A list of primers used in this study.

Table S3. Perseus output data.

Table S4. Raw data of proteomics.

Table S5. Publicly available data on the GPC levels of mesenchymal cells.

Table S6. *In silico* knockdown of *UGDH* in GEMs.

Table S7. Data of phosphoproteomics.

